Design of Microheater for Thermo-Optic Tuning of Silicon Photonic Filters

by

Ahmet Kağan Koral

A Dissertation Submitted to the
Graduate School of Sciences and Engineering
in Partial Fulfillment of the Requirements for
the Degree of

Master of Science

in

Electrical and Electronics Engineering

KOÇ
ÜNİVERSİTESİ

August 11, 2022

Design of Microheater for Thermo-Optic Tuning of Silicon Photonic Filters

Koç University

Graduate School of Sciences and Engineering

This is to certify that I have examined this copy of a master's thesis by

Ahmet Kağan Koral

and have found that it is complete and satisfactory in all respects,

and that any and all revisions required by the final

examining committee have been made.

Committee Members:

____

Assist. Prof. Emir Salih Mağden (Advisor)

____

Prof. Ali Serpengüzel [Co-Advisor]

____

Assoc. Prof. Onur Ferhanoğlu

____

Assist. Prof. Mehmet Cengiz Onbaşlı

____

Assist. Prof. Levent Beker

Date: ______________________________

Dedicated to my parents and my sister

ABSTRACT

Design of Microheater for Thermo-Optic Tuning of Silicon Photonic Filters

Ahmet Kağan Koral

Master of Science in Electrical and Electronics Engineering

August 11, 2022

Microheater is the small-scaled version of resistive heater and uses Joule heating for heat generation. Having a low footprint and power consumption has enabled the microheater to be used in many areas. High thermo-optic coefficient of silicon has allowed this structure to be used in silicon photonics studies. This work focuses on designing an efficient microheater for our photonic filters.

First, the appropriate microheater geometry was determined because the geometry of this structure has a crucial influence on the power consumption of the microheater and the temperature uniformity of the device to be heated. After the proper geometric structure has been chosen, the determination of the properties of this microheater is divided into two parts. These features play an essential role in reducing the temperature difference in the heated device. In the first part, the separation between the heater lines was determined. In the second part, the amount of overflow of the microheater on the device was designated. After specifying all features of the microheater structure, its electrical and thermal properties were investigated in the simulation environment. Finally, it was compared with the best-in-class microheaters, and the reasons for the performance differences were examined.

ÖZETÇE

Silisyum Fotonik Süzgeçlerin Termo-Optik Ayarı için Mikroısıtıcı Tasarımı

Ahmet Kağan Koral

Elektrik ve Elektronik Mühendisliği, Yüksek Lisans

11 Ağustos 2022

Mikroısıtıcı, dirençli ısıtıcının küçük ölçekli sürümüdür ve ısı üretimi için Joule ısıtma kullanmaktadır. Düşük kaplama alanına ve güç tüketimine sahip olması, mikroısıtıcının birçok alanda kullanılmasına olanak sağlamıştır. Silisyumun yüksek termo-optik katsayısı, bu yapının silisyum fotonik çalışmalarında kullanılmasına olanak sağlamıştır. Bu çalışmada, fotonik süzgeçlerimiz için verimli bir mikroısıtıcı tasarlamaya odaklanmaktadır.

İlk olarak, uygun mikroısıtıcı geometrisi belirlenmiştir çünkü bu yapının geometrisi, mikroısıtıcının güç tüketimi ve ısıtılacak aygıtın sıcaklık homojenliği üzerinde çok önemli bir etkiye sahiptir. Uygun geometrik yapı seçildikten sonra bu mikroısıtıcının özelliklerinin belirlenmesi iki bölüme ayrılır. Bu özellikler, ısıtılan cihazdaki sıcaklık farkını azaltmada önemli bir rol oynamaktadır. İlk bölümde ısıtıcı yolları arasındaki ayrım belirlenmiştir. İkinci bölümde ise mikroısıtıcının cihaz üzerindeki taşma oranı belirlenmiştir. Mikroısıtıcı yapısının tüm özellikleri belirlendikten sonra benzeşim ortamında elektriksel ve ısı özellikleri incelenmiştir. Son olarak sınıfının en iyi mikroısıtıcıları ile karşılaştırılmış ve başarım farklılıklarının nedenleri incelenmiştir.

ACKNOWLEDGEMENTS

I would like to express my gratitude and respect to my advisors Assist. Prof. Emir Salih Mağden and Prof. Ali Serpengüzel for providing me an opportunity to study at Koç University and for their help, guidance, and encouragement during my MSc degree study. I would also like to express my gratitude to the members of my thesis committee Assoc. Prof. Onur Ferhanoğlu, Assist. Prof. Mehmet Cengiz Onbaşlı, and Assist. Prof. Levent Beker for accepting to be part of my thesis defense and for their valuable feedback.

First and foremost, I would like to thank my parents and my sister for their love and support. They always supported and believed in me throughout my life. Also, I would like to thank my friends, who supported me, and were there, when I needed them.

I also wish to acknowledge members of Photonic Architecture Laboratories (PAL) and Microphotonics Research Laboratory (MRL) for their friendship and support. I can count myself lucky to have the privilege of working with them.

Finally, I would like to thank the Scientific and Technological Research Council of Turkey (TUBITAK) Grant #119E195 and TUBITAK 2210-National Scholarship Programme for MSc Students for their support and funding me during my graduate studies.

TABLE OF CONTENTS

LIST OF TABLES

LIST OF FIGURES

ABBREVIATIONS

Al_2O_3/Pt/Ta	Alumina/Platinum/Tantalum
BOX	Buried oxide
CMOS	Complementary Metal Oxide Semiconductor
CVD	Chemical Vapor Deposition
FSR	Free Spectral Range
IMEC	Interuniversity Microelectronics Centre
LPCVD	Low-Pressure Chemical Vapor Deposition
MEMS	Micro-electromechanical system
µm	Micrometer
µs	Microsecond
ms	Millisecond
NiCr	Nichrome
NiSi	Nickel monosilicide
nJ	Nanojoule
nm	Nanometer
NoC	Networks on Chip
ns	Nanosecond
PDK	Process Design Kit
PECVD	Plasma Enhanced Chemical Vapor Deposition
PVD	Physical Vapor Deposition
ROADM	Reconfigurable Optical Add-Drop Multiplexer
SiC	Silicon carbide
SiN	Silicon mononitride
Si_2N_2O	Silicon oxynitride
Si_3N_4	Silicon nitride
SiO_2	Silicon dioxide
SOI	Silicon on Insulator
SRRTF	Silicon Ring Resonator Based Thermally Tunable Filter
TiO_2	Titanium dioxide
USPS	Ultrasonic Spray Pyrolysis System
WDM	Wavelength Division Multiplexing

Chapter 1:
INTRODUCTION

1.1 Microheaters

Heaters are tools used to increase the temperature of their environment. Many substances in solid, liquid, or gaseous states have been used as heat sources for many years. In 1841, James Prescott Joule found that electricity could be used as a heat source [1]. In these studies, Joule discovered that a conductor carrying an electric current produces heat, and this was referred to as Joule's law in the literature. Since then, resistance heaters have been used in many fields such as engineering, science, and space. However, resistance heaters were consuming a lot of power and took up much space. With the advancement in the field of micro and nanotechnology, high power consumption and taking up too much space problems have been eliminated and resistance heaters started to be used in micro-electromechanical systems (MEMS) and photonics.

A microheater is the small-scale version of a resistance heater that generates heat by applying electrical current to a resistor. In addition to small footprint of microheater, a microheater provides many advantages, such as low power consumption and fast thermal response (between microseconds (µs) and milliseconds (ms)) [2]. An ideal microheater should have some physical, thermal, and electrical properties. Physically, a microheater must withstand high temperatures. In addition, microheater should be long-lasting, corrosion resistant and reusable. Electrically, microheater should have high heater resistance as well as low electrical power consumption. Thermally, microheater should have a low-temperature resistance coefficient along with high thermal conductivity [3]. In addition to physical, electrical, and thermal properties, the efficient operation of the microheater depends on the material properties and the design of the heater. However, the materials or geometrical design of the microheater varies according to the application in which the microheater will be used. Microheaters with different designs and materials are used in many applications, such as humidity sensors [4], gas sensors [5], fingerprint sensors [6], fuel cells [7], protein traps [8], wind sensors [9], and optical filters [10].

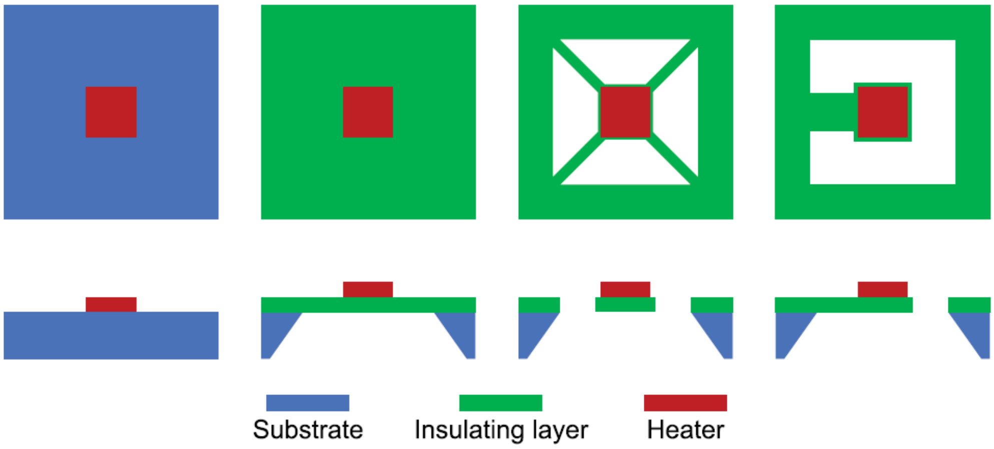

Figure 1.1: Top and cross-sectional view of four main designs of microheaters [11].

There are four main types of microheater designs. In the first style, the microheater is directly on the substrate [12][13]. In the second layout, between the substrate and the heater, there is an insulating layer (oxidation layer), and the second design is called a closed membrane [7][14]. In the third type, the microheater is positioned on the insulating layer, as in the closed membrane, but in the third structure, the insulating layer is only in the section where the microheater is located. Third design is called an open membrane [15][16]. The microheater is located on a cantilever made from the insulating layer in the last structure and this type is called as cantilever [17][18]. Figure 1.1 shows the top and cross-sectional view of these four different structures. The design to be used varies according to the applications to be made. However, among them, closed and open membrane ones are the most used designs.

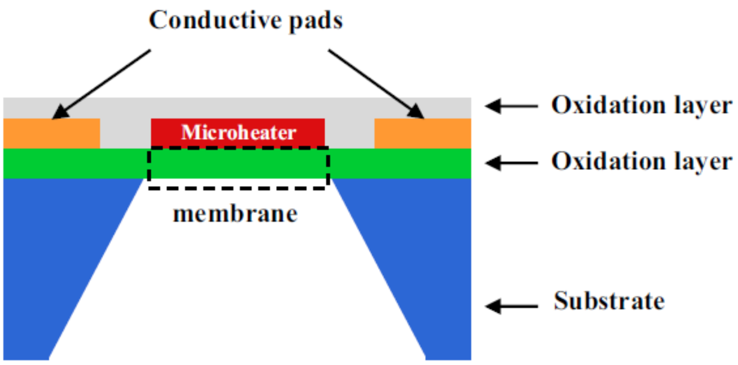

Figure 1.2: Cross-sectional view of a microheater [2].

An entire microheater structure consists of five components which are oxidation layers, resistive layer (or microheater), membrane, conductive pads, and substrate [2]. The cross-sectional view of a closed membrane type microheater is shown in Figure 1.2.

The oxidation layer is the surrounding layer of the microheater. Oxidations layers are made of insulating material to prevent the microheater from consuming more power [19]. In addition, the thermal conductivity is much lower than the resistive layer, so oxidation layers provide thermal insulation. The primary source of heating takes place in the resistive layer. The membrane is located between the resistive layer and substrate and creates thermal insulation between these two layers. This insulation reduces the power consumption of the microheater system [2]. The substrate serves as the microheater's base and the cavity in substrate depends on the applications. Some applications do not need a cavity in the substrate. Lastly, conductive pads are used for creating the electrical potential difference on the resistive layer.

1.1.1 Microheater Material

Picking the suitable material is critical for obtaining an efficient microheater because materials' electrical, physical, and thermal properties affect the microheater's power consumption and thermal behavior. As mentioned in the previous section of this chapter, an ideal microheater has some thermal, electrical, and physical characteristics. These features look independent from each other, but they reciprocally depend on the design factors and physics because thermal, electrical, and physical characteristics are primarily derived from the material properties of components, that are used in a microheater system.

Resistive Layer Materials

The material to be used in the resistive layer must survive in corrosive environments and high operating temperatures. Furthermore, the material's resistance should change minimally during temperature change, and should be able to dissipate the generated heat quickly. Metals, semiconductors, and ceramics are preferable material types for the heating layers in microheaters [2]. Among these, microheaters made from metal are the most used in the literature because metals provide convenience in the geometric design of the metal microheater [11]. Moreover, because metals have lower resistivity values than semiconductors and ceramics, microheaters made from metal operate at lower voltages and respond quickly. Because of high melting temperatures of metals, metal heaters operate in a broader temperature range and have a longer lifetime. Platinum (Pt), Aluminum (Al), Nickel (Ni), Titanium (Ti), Tungsten (W), Chromium (Cr), Gold (Au), and Silver (Ag) are the most common metals used for resistive layer. Table 1.1 shows the material properties of the most common metal microheater materials at room temperature.

Table 1.1: Material properties of the different microheater metals.

Material	Pt	Al	Ni	Ti	W	Cr	Au	Ag
Melting Point (°C)	1772 [20]	660 [20]	1455 [20]	1680 [20]	3387 [20]	1845 [20]	1063 [20]	962 [20]
Thermal conductivity (W/mK)	71.6 [20]	237 [20]	90.7 [20]	21.9 [20]	174 [20]	93.7 [20]	317 [20]	429 [20]
Resistivity ($\times 10^{-8}\Omega$m)	10.7 [21]	2.65 [21]	6.99 [21]	54.3 [22]	5.6 [21]	13 [21]	2.35 [21]	1.59 [21]

Membrane Materials

Silicon dioxide (SiO_2) and silicon nitride (Si_3N_4) are the most common materials that are preferable for the membrane layer [2]. Silicon carbide (SiC), thin Si layer, porous silicon, and silicon oxynitride (Si_2N_2O) are the other materials that are used as membrane materials [23].

Oxidation Layer Materials

SiO_2, titanium dioxide (TiO_2), and alumina/platinum/tantalum (Al_2O_3/Pt/Ta) are the most preferrable materials for the oxidation layers [2][19].

Conductive Pad Materials

Au, Ni, and Ag are the most common materials used to make conductive pads [2]. The conductive pads' electrical resistivity should be low in contrast to the heating element, so that more efficient Joule heating happens at the heater resistor. In addition, unwanted heating of the pads is prevented [3].

Substrate Materials

Silicon (Si), glass, ceramics, and stainless steel are the most typical materials for the substrate. Substrates made of steel or glass are not as resistant to high temperatures as substrates made of silicon or ceramic [2][19]. Among the common materials, the substrate is frequently made from Si because Si substrate can work at high temperatures for extended periods of time and has high thermal conductivity [24].

1.1.2 Microheater Design

The mechanical and electrothermal design of a microheater has a critical role in microheater development because mechanical and electrothermal designs have a major impact on the homogeneous temperature distribution on the heated device and the power consumption of the microheater [23].

Geometry

The microheater's design geometry is crucial for achieving low power consumption and efficient temperature homogeneity across the heated device. The physical dimensions and material type of the microheater affect heater's resistance. The resistance of the microheater can be found by the following equation:

$$R = \frac{\rho \ell}{A} \tag{1.1}$$

In Equation (1.1), A denotes the cross-sectional area (width × thickness) of the resistor, ρ is the resistivity of the material, and ℓ is the resistor length. The shape of the microheater varies in applications, from simple patterns to complex patterns. For optimal heating, microheaters usually need to be precisely at the top of the structure to be heated, and cover most of the structure. Researchers designed, investigated, and fabricated various microheater designs and some of these designs are illustrated in Figure 1.3.

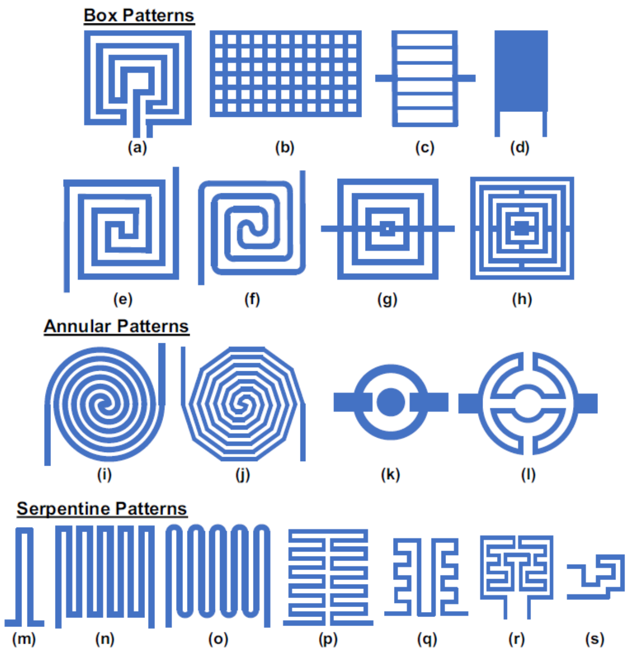

Figure 1.3: Various microheater design structures designed by researchers (a) Inverted C-shaped (b)Rectangular mesh pattern (c) Lines (d) Plate (e) Double spiral square (f) Curved double spiral square (g) Ring-shaped (h) Square grilled (i) Double spiral (j) Octogen (k) Circular (l) Dual C (m) Inverted U (n) Meander (o) Meander with rounded corners (p) Dual meander (q) U Dual meander (r) Wing (s) Hook [3].

According to Jeroish et al., among these designs, fan type, meander, and double spiral square have the least power consumption [3]. Moreover, the best temperature distribution profile was observed in the meander and double spiral heaters [3]. According to Lekshmi et al. and Utomo et al., the thermal distribution of the meander heater was slightly better than the spiral square model [25][26]. In another study, Sujatha et al. made simulations in COMSOL Multiphysics to find the optimal design of a microheater [27]. In these simulations, Sujatha et al. compared single meander, double meander, fan shape, and square shape designs [27]. The square shape design is their own design. Sujatha et al. obtained square-shaped heater by randomly removing squares from a large square [27]. As a result of these simulations, it has been observed that a meander-type heater produces a better uniform temperature distribution than double meander and fan shape. In addition, the square-shaped heater provided the best temperature homogeneity [27].

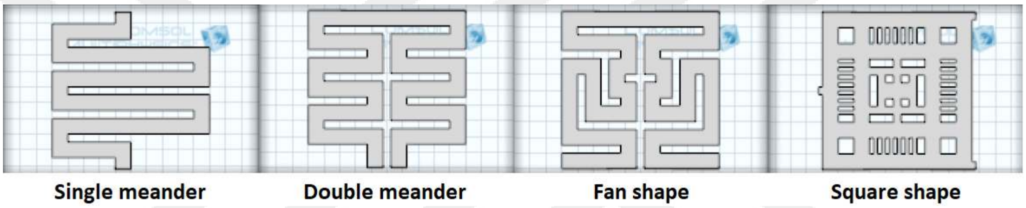

Figure 1.4: Sujatha et al. designs for comparison [27].

Thermal Loss

In addition to the microheater geometry, the power consumption of a microheater depends on heat loss. Conduction, convection, and radiation are a microheater device's primary sources of heat loss [28]. Conduction heat loss takes place through the membrane, over the electrical connections, and via the air. Heat transfer through radiation happens via electromagnetic radiation within a void or air-filled medium. Lastly, convection heat loss occurs through the air. The dissipation of heat in a microheater is depicted in Figure 1.5.

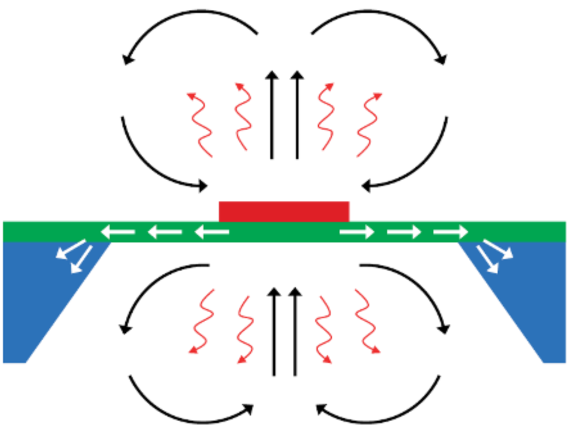

Figure 1.5: Schematic diagram of heat transfer in a microheater [11].

In this illustration, white arrows represent conduction through the membrane, red curly arrows are heat transfer due to radiation and black arrows show conduction through the air and air convection. The total heat loss can be calculated using the formula below [23]. In this equation, the first term describes the heat conduction through the membrane, the second represents the air conduction, the third term is heat losses due to radiation, and the remainder is the convection loss.

$$Q_{tot} = G_m \lambda_{\mathrm{m}} (T_{hot} - T_{amb}) + G_{air} \lambda_{air} (T_{hot} - T_{amb}) + G_{rad} \sigma \epsilon (T_{hot}^4 - T_{amb}^4) + \Delta x$$

G_m, G_{air} and G_{rad} are the geometric factors related to the membrane or device design. T_{hot} is the temperature of the microheater, T_{amb} is the ambient temperature. λ_m, λ_{air} are the thermal conductivity of the membrane and the surrounding air, ϵ is surface emissivity, and σ is the Stefan-Boltzmann constant.

In a microheater system, the primary heat loss mechanism occurs in the form of conduction through the membrane as the heater is directly connected to that layer. According to Spruit et al., heat loss through the electric contacts is also significant because their thermal conductivity is much higher than other parts, but this loss is usually not considered [11]. According to Bhattacharyya and Simon et al., in most designs, heat loss due to air convection is ignored because of the heater's small size [23][29]. Many microheaters do not reach high temperatures that's why in most of the literature heat losses from thermal radiation emission are neglected [11]. On the other hand, researchers must be cautious when microheater temperature reaches high values because there is a T^4 dependence on the radiation heat loss, as seen in the total heat loss equation [23].

1.1.3 Microheater Fabrication

Microheater production is the last process before the heater is used in practice. Over the years, microheaters have been produced by many different methods. Ultrasonic spray pyrolysis system (USPS) [30], electrochemical deposition [31], physical vapor deposition (PVD) [32][33], chemical vapor deposition (CVD) [34], etching [35], and printing [36], [37] are the most common and adapted techniques of microheater fabrication [3].

Ultrasonic Spray Pyrolysis System

Gharesi et al. designed a microheater made of tin oxide using this method [30]. The alumina substrate on which the tin oxide will be deposited is first washed with acetone. Then, substrate is rinsed with deionized water and left to dry on a hot plate. Aerosol droplets produced from precursor, which is a special solution, by using a piezoelectric transducer are transported to the collection chamber by gas. These transported droplets accumulate on the surface of the alumina substrate, and deposition occurs. Figure 1.6 shows the USPS schematic and fabrication process.

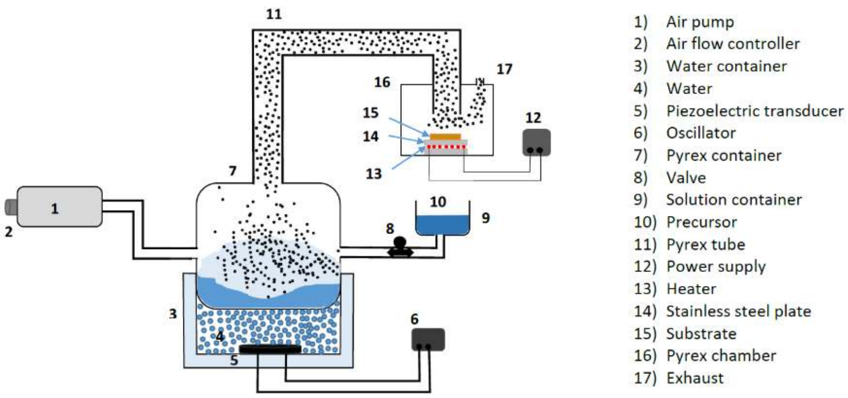

Figure 1.6: Schematic diagram of USPS [30].

Electrochemical Deposition

In this method, metal is deposited on a substrate by a simple electrolysis method. The positive electrode of the electrolytic cell device contains the coating material. On the opposing end, there is a heater design to be coated, and these electrodes are immersed in an ionic component. Conducting ions are deposited on the cathode tip by passing an electric current directly through the system [31].

Physical Vapor Deposition

Evaporation and sputtering techniques are classified as the PVD method. The source material and substrate are placed in a vacuum chamber filled with sputtering gas in the sputtering process. Plasma is formed by sputtering gas ionization, and bombards the source material to expel atoms when a large potential difference is applied between the source and the substrate. The heater is formed by depositing the ejected particles on the substrate. There are several types of evaporation techniques, such as thermal evaporation and e-beam evaporation. In the e-beam evaporation method, the material to be coated is evaporated first by using electron beam bombardment or thermal energy in a vacuum environment. Then the evaporating atoms gradually condense on the coated material [3]. In the thermal evaporation method, the material to be coated is evaporated utilizing high temperatures in the vacuum environment. Moving vapor particles accumulate on the substrate, and coating takes place [38].

Chemical Vapor Deposition

CVD is the process of depositing a thin coating on a substrate by reacting chemical gas or volatile liquids with an external activation energy source. A uniform deposition is made on a larger area without pollution, and defect with the CVD method. On the other hand, this method consumes a lot of power, and requires a high temperature for deposition [3].

Etching

Etching is a method of chemically removing a component or later from a wafer's surface using a suitable etchant. During the etching process, a substance that resists etching covers a portion of the wafer from the etchant. This substance is usually a photoresist that has been patterned via photolithography. The parts outside the photoresist area also dissolve.

Printing

With the printing method, the heater geometry is drawn on the surface. Therefore, etching chemicals are not used in printing technique. Screen printing and micro pen direct writing are some printing methods adapted to manufacture microheaters. In the screen-printing method, the desired heater shape is first printed on a transparent sheet. This sheet is then placed on the screen and exposed to ultraviolet light. Then, the screen on which the heater surface has been treated is cleaned and filled with ink. Finally, microheater is printed on the substrate with the help of a squeegee [36]. In the micro-pen direct writing technique, the design is drawn on the substrate with a special pen with a Pt paste on the tip. During writing process, the substrate heat with a convection oven, to remove organic components in the paste. Then, a continuous-wave laser scans, and sinters the drawn heater pattern. Lastly, an organic solvent removes the un-sintered paste, and forms the microheater [37]. Figure 1.7 shows the illustration of the micro-pen direct writing technique.

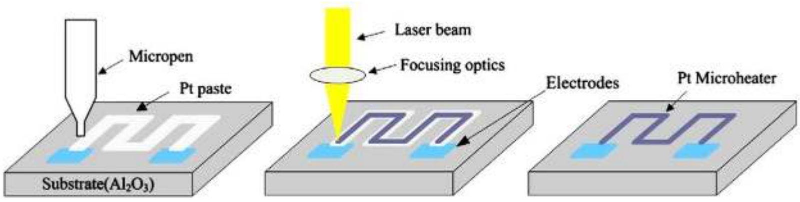

Figure 1.7: The illustration of the micro-pen direct writing method [37].

1.2 *Thesis Organization*

This complete thesis has been presented in three chapters, excluding Chapter 1 for Introduction and Chapter 5 for Conclusion.

Chapter 2 covers the review of the best-in-class microheaters used in silicon photonics studies. This chapter focuses on the designs and the performances of microheaters used in different studies in the field of silicon photonics.

Chapter 3, firstly, presents the simulation environment and materials that have been used in these simulations. Next, chapter 3 focuses on the performances of microheaters with different design structures for deciding on the optimum microheater geometry. Then, this chapter presents the studies and results on the optimization of the geometric properties of the microheater to be used. After all the properties of the microheater are determined, the electrical and thermal properties of the design are examined in the simulation environment. Finally, it describes pre-fabrication and the fabrication steps of the designed microheater.

Chapter 4 compares our design with best-in-class microheaters in the literature. These comparisons focus on the efficiency of the microheaters and examine the factors that cause these performance differences.

Chapter 2:
REVIEW OF BEST-IN-CLASS MICROHEATERS IN PHOTONICS

This section describes the features and performances of best-in-class microheaters in the literature. Chapter 2 also provides performance metrics and the main claimed novelties of these studies.

The reconfigurability of photonic integrated devices and circuits allows control of the tuners, thus providing miscellaneous functionality in many applications such as optical signal processing, photonic networks [39]. Due to their compatibility with the complementary metal-oxide-semiconductor (CMOS) fabrication process, thermo-optic effect and electro-optic effect are the most common approaches used in the reconfiguration of Si photonic devices [40]. The thermo-optic effect is preferred over the electro-optic effect, as thermo-optic tuning consumes less power and provides a broader adjustment range [40]. Moreover, due to silicon's high thermo-optic coefficient ($1.86 \times 10^{-4} K^{-1}$) temperature changes have a significant impact on Si devices [41], and this can be an another reason why the thermo-optic effect is preferred over electro-optic effect. Another reason is silicon has a small thermal expansion coefficient ($2.57 \times 10^{-6} K^{-1}$) because low thermal expansion coefficient shows that silicon expands at a minimum rate with temperature changes [42]. The only drawback of the thermo-optic effect is its slow response time because of the slow heat diffusion process on silicon on insulator (SOI) [42]. A good thermo-optic heater must be able to tune the Free Spectral Range (FSR) to the greatest possible value while using the least amount of power. Short definition of FSR is the distance between two successful resonant wavelengths. The photonic circuits can function across a wide bandwidth because of the vast tuning range. Many studies have been done over the years using thermo-optic tuning. Table 2.1 shows the properties of the microheaters used in these studies. In Table 2.1, Device & Heater Contact column shows the connection between heater and device. Gap means there is a SiO_2 layer between microheater and device to be heated, and direct represents the direct connection between the heater and the device. Heat isolation column shows whether thermal insulation is provided in the system with air trenches. Table 2.2 summarizes and compares the performances of these microheaters.

Table 2.1: Best-in-class microheater properties.

Microheater	**References**	**Microheater Cross Section ($w \times$ h) (in μm)**	**Microheater Material**	**Device & Heater Contact**	**Heat Isolation**
I	Gan et al. [43]	$0.8 - 1 \times 0.1$	Ti	Gap	No trench
II	Geng et al. [44]	1×0.2	Ti	Gap	No trench
III	Dong et al. [45]	1×0.1	Ti	Gap	Isolation trench
IV	Dong et al. [46]	1×0.1	Ti	Gap	Isolation trench
V	Fang et al. [47]	Not Given	Nickel monosilicide (NiSi)	Direct	Isolation trench
VI	Kim et al. [48]	1×0.1	Cr	Gap	No trench
VII	Atabaki et al. [42]	1×0.1	Ni	Gap	No trench
VIII	Atabaki et al. [40]	0.4×0.1	Nichrome (NiCr)	Direct	No trench
IX	Sherwood-Droz et al. [49]	1×0.3	NiCr	Gap	No trench

2.1 Microheater I

Gan et al. reported an efficient silicon microring resonator with the broadest thermo-optic tuning to date in that year [43]. They fabricated a microheater with an annular pattern with Ti as the heater material. The thickness of the heater was 0.1 micrometer (μm), and the width varied between 0.8 and 1 μm. Gan et al. set the spacing between the heater wires to 0.8 μm to be fabricated compatible and covered the microheater with a

0.1 µm thick SiO_2 layer to prevent oxidation at high operating temperatures [43]. The designed microheater was placed 900 nanometer (nm) above the 7 µm radius silicon microring resonator with a cross-sectional area of 0.6 µm × 0.106 µm to reduce the optical loss due to metal heater wires. Figure 2.1 illustrates the fabricated microheater on top of the ring resonator.

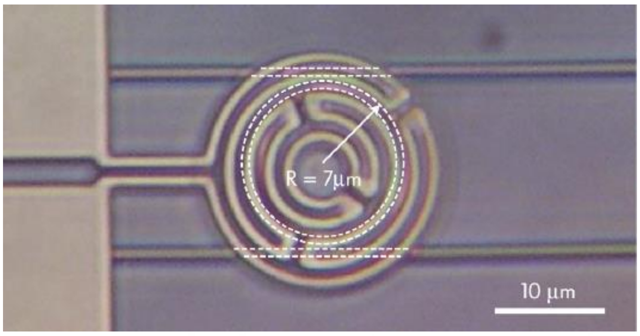

Figure 2.1: Designed and fabricated microheater on the ring resonator [43].

In order to cover half of the C band, Gan et al. have created the microring filters with a 16 nm FSR [43]. Gan et al. demonstrated that with an average tuning efficiency of 28 µW/GHz, the tuned wavelength changes by 10 nm and shifts by 20 nm with an average efficiency of 17 µW/GHz [43], as seen in Figure 2.2. As can be seen in more detail in Table 2.2, the microheater consumes 56 mW for an FSR shift.

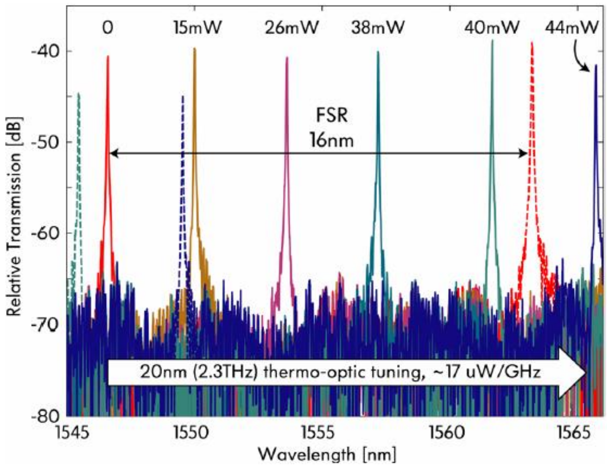

Figure 2.2: Spectra of drop-port transmission at various tuning powers [43].

Performance Metrics: Gan et al. achieved an efficiency of 28 µW/GHz (56 mW/FSR) with 16 nm FSR [43].

Main Claimed Novelty: Gan et al. reported the broadest full-FSR thermal tuning in silicon photonics at that time [43].

2.2 *Microheater II*

Geng et al. designed a four-channel reconfigurable optical add-drop multiplexer (ROADM) based on a silicon photonic wire waveguide that can be controlled by the thermo-optical effect [44]. In this study, Geng et al. referenced and optimized the heater structure used by Gan et al. [43]. Geng et al. used the same annular microheater pattern and produced it from Ti [44]. The only difference between the two microheater designs was that they just increased the heater thickness from 0.1 µm to 0.2 µm. The size of the device was 1000 µm × 500 µm. The designed microheater was placed on the silicon microring resonator with 5 µm radius and cross-sectional area of 0.3 × 0.3 μm^2. Figure 2.3 shows their design.

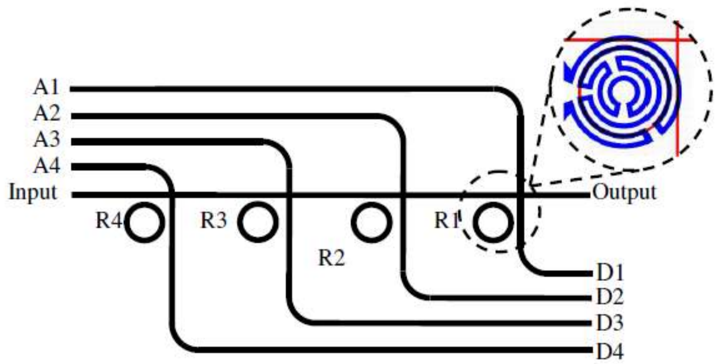

Figure 2.3: The schematic of the four-channel ROADM [44].

As can be seen in more detail in Table 2.2, the tuning efficiency of the microheater is about 6.187 mW/nm. In a half C band with adjacent channel spacing of 1.6 nm, their device may add/drop any four optical channels, and the tunable bandwidth covers around 17 nm [44].

Performance Metrics: Geng et al. achieved tuning power consumption is around 6.187 mW/nm [44].

Main Claimed Novelty: Geng et al. discovered that as the applied voltage increases, the waveguide signals' polarization changes, while the states of other equipment remain stable [44]. They called it the thermo-optic polarization rotation. As Geng et al. stated this is the first study that the thermo-optic polarization rotation reported [44].

2.3 Microheater III

Dong et al. demonstrated a thermally reconfigurable multiplexing device based on silicon microring resonators with low tuning power and minimal thermal crosstalk [45]. Dong et al. obtained these outcomes by adding air trenches close to the ring waveguides [45]. Air trenches prevented the heat leakage in the horizontal directions. The device consists of cascaded micro-ring resonators. The waveguide width and thickness were set as 0.45 µm and 0.25 µm, respectively. Microring resonators were racetrack-shaped with a 4 µm bending radius and 2 µm straight coupling length. A racetrack-shaped microheater made of Ti with a cross-sectional area of 1 µm x 0.1 µm was placed at 1.2 µm above the ring resonator. The second layer of SiO_2 was deposited on the heater with a 0.5 µm thickness. Figure 2.4 shows the constructed (de)multiplexers and the cross-section of the ring waveguide.

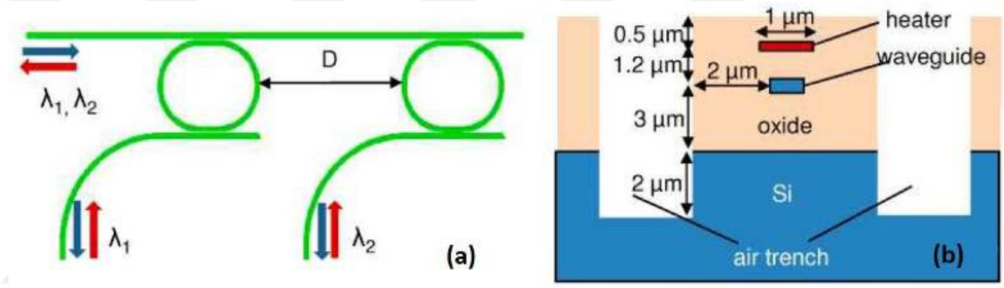

Figure 2.4: (a) Constructed (de)multiplexer from cascaded microring resonators, (b) cross-section of the ring waveguide with air trenches [45].

Dong et al. applied the heating power only on the first ring [45]. For comparison, Dong et al. fabricated and tested devices with and without air trenches [45]. For both devices, the ring spectra revealed an FSR of 19 nm, and these spectra are shown in Figure 2.5.

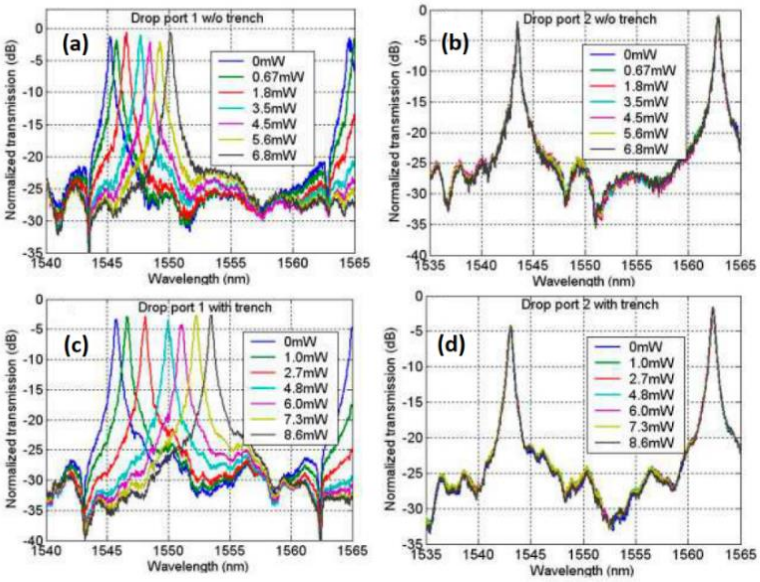

Figure 2.5: (a) Spectra of drop port 1 without trench, (b) spectra of drop port 2 without trench, (c) spectra of drop port 1 with trench, (d) spectra of drop port 2 with trench [45].

Dong et al. determined the resonance wavelength by applying different powers by using the spectra of drop port 1 for both devices [45]. After applying linear fitting to resonance shift values, Dong et al. achieved the results illustrated in Figure 2.6 [45]. According to the linear fitted results, the tuning efficiency of the devices with and without air trenches was obtained as 1.1 mW/nm and 1.42 mW/nm, respectively. For one FSR shift for devices with and without air trenches, they achieved tuning power of 21 mW and 27 mW, respectively.

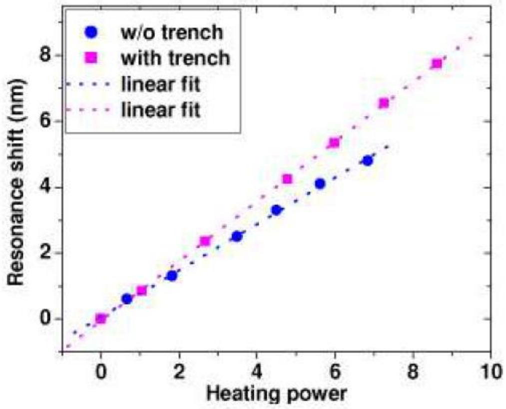

Figure 2.6: Heating power versus resonance shift [45].

The paper concludes that the thermally tuned cascaded microring provides two significant benefits over other types of silicon wavelength division multiplexing (WDM) devices, such as grating-based and MZI-based. Firstly, because each ring may be controlled separately, Dong et al. can be adjusted in terms of center wavelengths and channel spacing [45]. Second, microrings are much more compact devices [45].

Performance Metrics: Dong et al. achieved low tuning power (20.9 mW/FSR) and negligible thermal crosstalk for rings separated by 15 µm [45].

Main Claimed Novelty: Dong et al. designed thermally reconfigurable multiplexing devices based on silicon microring resonators with thermal isolation trenches that had minimum tuning power and thermal crosstalk [45].

2.4 *Microheater IV*

Dong et al. have reported a tunable racetrack resonator that consumes minimum power per FSR [46]. The factor distinguishing this work from their previous work [45] is the undercuts under the resonator. To reduce the power consumption of the microheater, Dong et al. etched away the substrate after forming air trenches [46]. This study used a racetrack-shaped heater made of 1 µm wide and 0.1 µm thick Ti and placed microheater at 1.2 µm above the racetrack resonator with a cross-section of 0.45 µm x 0.25 µm. A cross-sectional view of the ring resonator with undercuts is demonstrated in Figure 2.7.

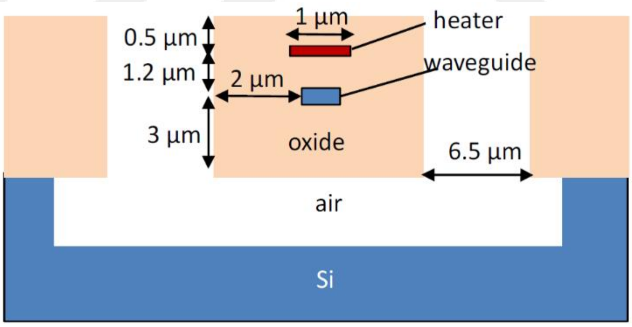

Figure 2.7: Cross-sectional view of the ring resonator with undercuts [46].

Dong et al. fabricated two racetrack resonators with straight coupling lengths of 11 µm and different bending radii as 4 µm and 10 µm [46]. Figure 2.8 illustrates the spectra of the FSRs of 11.5 nm and 6.4 nm for the device with 4 µm and 10 µm bend radii, respectively. For one FSR shift, 2.4 mW of tuning power is required for both resonators. The wavelength tuning efficiency for both devices was estimated to be 4.8 nm/mW and 2.7 nm/mW for 4 µm bend radius and 10 µm bend radius racetrack rings, respectively. When Dong et al. compared their results with their previous results, it was seen that devices with undercut consume an order of magnitude less power for an FSR shift than devices without undercut [46]. According to the results, the undercut structure provided crucial efficiency in the power consumption but significantly decreased the tuning speed [46].

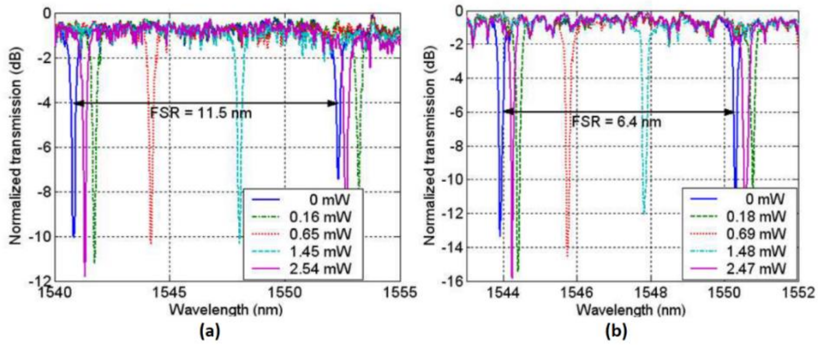

Figure 2.8: Through port spectra with various power of (a) 4 µm bend radius, (b) 10 µm bend radius [46].

Performance Metrics: Dong et al. achieved ultralow tuning power (2.4 mW/FSR) [46].

Main Claimed Novelty: Dong et al. reported an ultralow tuning power of 2.4 mW per FSR by using undercuts beneath the racetrack resonators [46].

2.5 *Microheater V*

In their study, Fang et al. designed and fabricated a ring resonator filter with high efficiency and ultra-fast temperature rise response [47]. The device is based on a ridge waveguide with NiSi microheater, which surrounds the slab region of the ring. Fang et al. used two different designs in this study [47]. Both structures consist of a 0.5 µm wide and 0.22 µm thick silicon ring resonator with around 16 µm diameter with a 200 nm gap between the ring and the bus waveguide. The distance between the ring waveguide and NiSi microheater is set as 1 µm to minimize the absorption loss. The only difference between both designs is that in the first design, there is an air isolation trench between the device and the Si substrate, as in the work of Dong et al. [46], there is no such air channel in the second structure. Figure 2.9 demonstrates the cross-sectional schematic of the tunable ring resonator filter with an air isolation trench. Both devices were fabricated on an 8-inch SOI wafer with a 2 µm thick buried oxide (BOX) layer and 220 nm thick top Si layer.

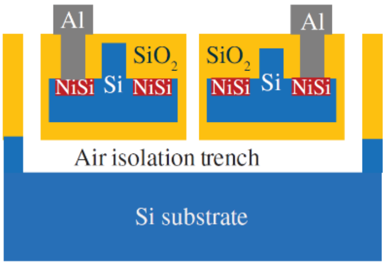

Figure 2.9: Cross-sectional view of the tunable ring resonator filter with air isolation trench [47].

For both designs, the measured FSR was 12.5 nm. The applied DC voltages for ring-resonator filters with and without an air separation trench were 1.7 V and 5.7 V, respectively, for one FSR wavelength shift. Fang et al. calculated that the power consumption of these microheaters were 4.9 mW and 59.2 mW for with and without air isolation, respectively, which showed that the air isolation trench reduced the power consumption by 92% [47]. From these results, the necessary power for the one-nanometer wavelength shift was calculated as 0.38 mW and 4.6 mW, respectively. The spectra and the power consumption of these filters are illustrated in Figure 2.10.

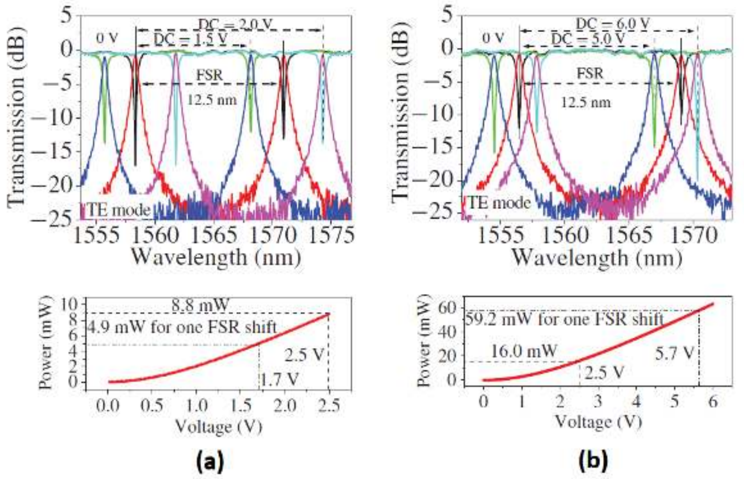

Figure 2.10: Power spectrums and power consumption graphs of filters: (a) with isolation trench, (b) without isolation trench [47].

Using Equation 2.1, Fang et al. found the relationship between the temperature change and the power consumption [47].

$$\frac{\Delta W}{\Delta T} = \frac{\Delta \mathrm{W}}{\Delta \lambda} \cdot \frac{\Delta \lambda}{\Delta \mathrm{T}} \quad (2.1)$$

In this equation, ΔW and Δλ are the increments of consumed power and wavelength and represent the consumed power and the FSR value, respectively. Since Si thermo-optic coefficient value is around $1.86 \times 10^{-4} K^{-1}$, the $\frac{\Delta\lambda}{\Delta T}$ value is equal to $7.66 \times 10^{-2} nm/K$

[47]. When the obtained results and equation (2.1) are used, the amount of power required for 1 K temperature change in devices with and without air insulation trench is calculated as 2.91×10^{-2} mW and 3.52×10^{-1} mW, respectively. The paper concludes that the microheater located on Si slabs improves the temperature-rise response, and the air isolation trench reduces the consumed power while heating the device.

Performance Metrics: Fang et al. achieved 0.38 mW of power consumption for 1 nm wavelength shift [47].

Main Claimed Novelty: Fang et al. reduced the power consumption by 92% by using the air isolation trench compared to the structure without the air isolation trench [47]. Furthermore, their design showed an ultra-fast temperature-rise response of 1.25 μs by forming microheaters in the Si slab region [47].

2.6 *Microheater VI*

Kim et al. have worked on a high-speed interrogation system based on a silicon-ring-resonator-based thermally tunable filter (SRRTF) [48]. Kim et al. reported a 100 kHz high-speed interrogation system based on that filter [48]. The width and the thickness of the waveguide were set as 450 nm and 220 nm, respectively and the radius of the ring was set as 2.5 μm. An omega-shaped microheater made of Cr with a cross-sectional area of 1 μm x 0.1 μm was fabricated at 1 μm above the ring resonator. The cross-sectional view of this device and the Cr microheater on the ring resonator have shown in Figure 2.11.

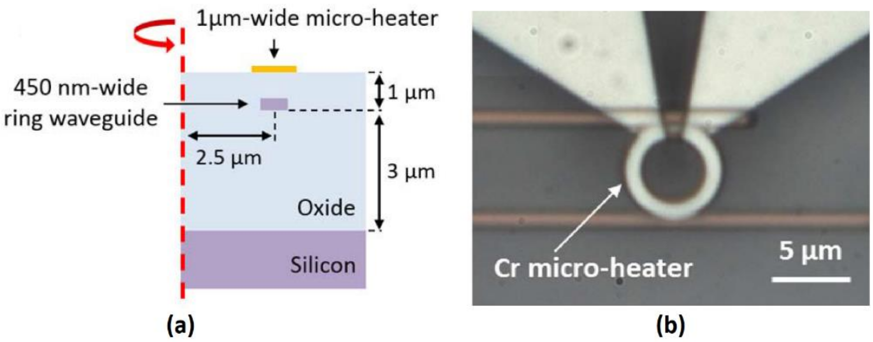

Figure 2.11: (a) Cross-sectional view of the SRRTF structure, (b) Cr microheater on the Si ring resonator [48].

The FSR of the SRRTF and the resonance wavelength were obtained at room temperature as 35.37 nm and 1535.49 nm, respectively. The wavelength tuning efficiency was calculated as 1.21 nm/mW. Figure 2.12 shows the transmission spectrum of the fabricated device and resonance wavelength as a function of heating power.

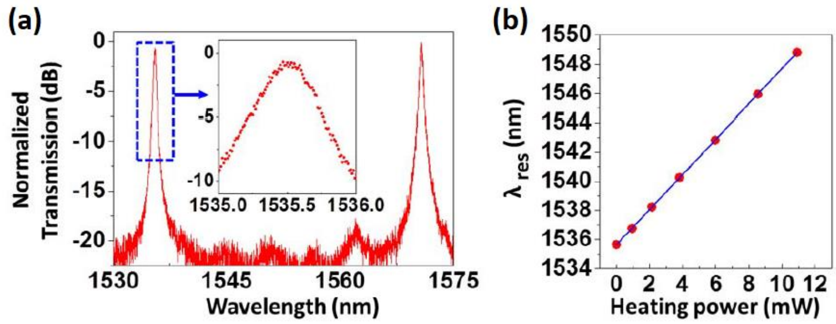

Figure 2.12: (a) Transmission spectrum of the SRRTF, (b) Wavelength of resonance as a function of heating power [48].

Performance Metrics: Kim et al. reported the wavelength tuning efficiency as 1.21 nm/mW [48].

Main Claimed Novelty: Kim et al. theoretically and experimentally investigated a high-speed sensor interrogation system using an SRRTF [48]. In thermal response time, the system scanned the entire spectral range. Also, they successfully demonstrated the interrogation of a temperature sensor at 100 kHz. Kim et al. stated that this work would pave the way for creating portable, small optical sensor devices for real-time monitoring of dynamic parameters [48].

2.7 Microheater VII

In their computational and experimental studies, Atabaki et al. examined the impact of various geometrical factors on increasing the reconfiguration speed of the thermally modified Si photonic devices [42]. A small piece of the architecture of the waveguide-microheater setup on an SOI substrate used in this study is shown in Figure 2.13. The width and thickness of the waveguide used in this study were chosen as 480 nm and 220 nm, respectively. A Ni-made microheater with a cross-sectional area of 1µm x 0.1µm was placed at 1 µm above the waveguide to increase the system temperature. There is a 1 µm thick SiO_2 cladding layer between the microheater and the device.

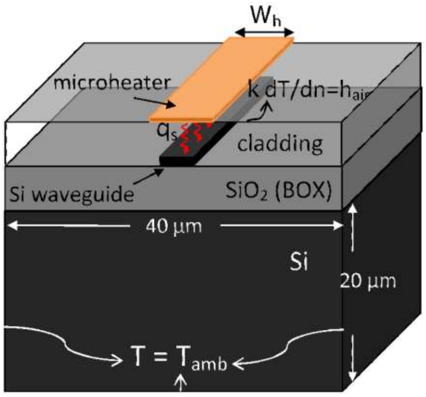

Figure 2.13: 3D architecture of the microheater over the waveguide [42].

Atabaki et al. did their experiments on a ring resonator with a diameter of 20 µm with a microheater on it [42]. Firstly, they studied the effect of the microheater width on the reconfiguration time. The results obtained in this study are shown in Figure 2.14 (a). Atabaki et al. observed that as the width of the microheater increased the temperature increase was less [42]. As a result of the increased heating volume, the reconstruction time increased as the width of the microheater increased. After these results, Atabaki et al. was understood that the microheater width does not have a significant effect on the reconfiguration time [42].

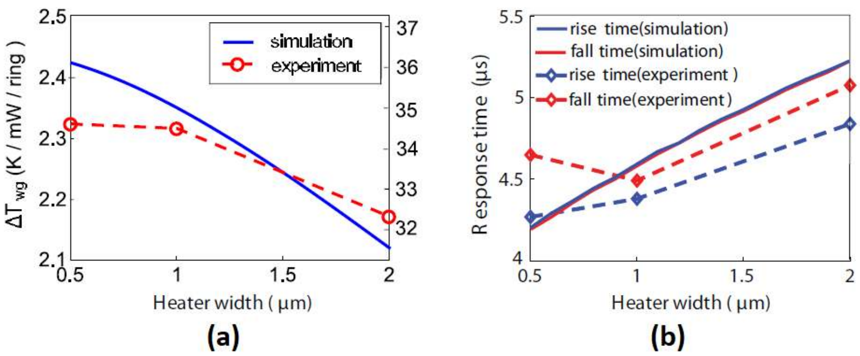

Figure 2.14: (a) Simulation and experimental findings for temperature rise in the core of the microring versus microheater width, (b) Simulation and experimental results of rise-time and fall-time of microheaters versus microheater width [42].

Another critical factor examined was the cladding material's effect on the microheater's performance. In this study, Atabaki et al. used plasma-enhanced chemical vapor deposition (PECVD) for SiO_2 deposition and low-pressure chemical vapor deposition (LPCVD) for silicon nitride (SiN) deposition as cladding materials [42]. The thermal conductivity of SiN is higher than SiO_2. When Atabaki et al. examined the obtained results, Atabaki et al. saw that the microheater's reaction became faster as the thermal conductivity of the cladding material increased [42]. However, Atabaki et al.

observed that as the thermal conductivity of the cladding material increased, the microheater consumed more power [42]. As a result, it has been measured that SiN cladding shortens the reaction time of the microheater but consumes 35% more power than SiO2 cladding [42].

Performance Metrics: In the article in which this study was published, no results were stated about the performance of the microheater. In a study Atabaki et al. published later, it was reported that this microheater consumed 3.6 mW of power at 1 nm wavelength shift [40].

Main Claimed Novelty: Atabaki et al. experimentally achieved ~4 µs rise/fall times through geometrical optimization [42]. Also, Atabaki et al. observed that LPCVD SiN cladding improves the reconfiguration speed by 20% compared to the conventional SiO_2 cladding [42].

2.8 *Microheater VIII*

Atabaki et al. reported another study on the reduction of reconfiguration time. This study reduced the reconfiguration time of the silicon photonic devices to fewer than 100 nanoseconds (ns) [40]. The schematic of the microdisk resonator coupled to a waveguide with the two microheater configurations is shown in Figure 2.15. This study used microheaters made of NiCr with a cross-sectional area of 0.4 µm x 0.1 µm called Type I and Type II. Type I microheater is placed 1 µm above from the microdisk by a cladding layer. The microheater, called Type II, was placed directly on the microdisk with a diameter of 5 µm and a thickness of 0.22 µm. Atabaki et al. placed Type II microheater directly on the microdisk without worrying about optical loss because optical mode dissipates in the center of the microdisk [40].

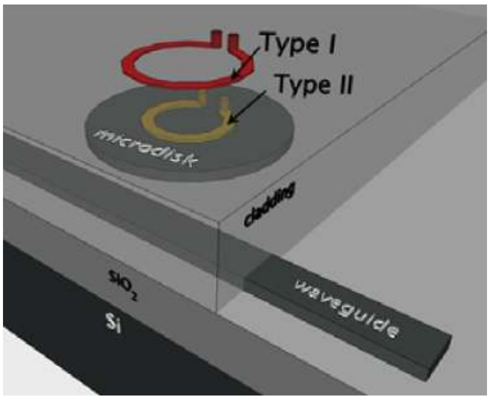

Figure 2.15: Schematic of the structure with Type I and Type II microheaters [40].

First, the system was modeled. The results obtained from the simulations are shown in Figure 2.16. The red curve in Figure 2.16(b) illustrates the temperature rise in the microdisk for a 1 nanojoule (nJ) impulse dissipated from the Type I microheater. Atabaki et al. observed the heat-propagation delay (δ_{HPD}), which is the delay that heat impulse reaches to the optical mode in Si, time as 840 ns [40]. When Atabaki et al. simulated the impulse response of the microdisk temperature for the Type II microheater, they observed δ_{HPD} as 19 ns [40].

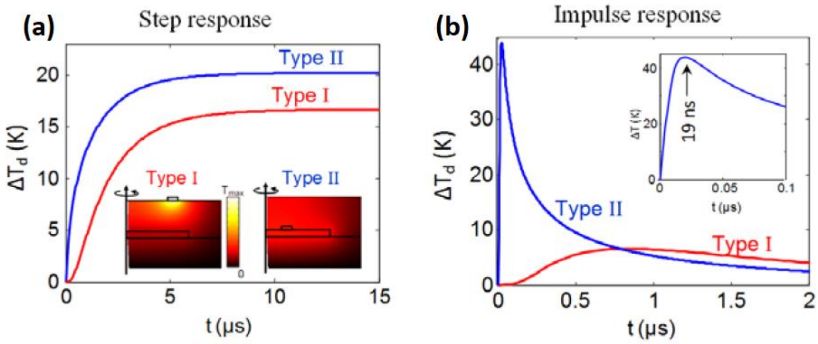

Figure 2.16: (a) Modelling result of the step response of the microdisk for 1mW power dissipation from Type I and Type II microheaters, (b) the step response of the microdisk for 1 nJ impulse dissipation from Type I and Type II microheaters [40].

In the measurements made on the fabricated device, Atabaki et al. measured the tuning efficiency value as 0.68 mW/nm [40]. Furthermore, Atabaki et al. fabricated a similar filter with a 4 μm diameter microdisk. In the results obtained after the measurements, the amount of power consumed by this device for 1 nm shift was measured as 0.48 mW. After the observations, the δ_{HPD} of the fabricated device was approximately 85 ns.

Performance Metrics: Atabaki et al. achieved 2.06 nm/mW wavelength tuning efficiency value [40].

Main Claimed Novelty: Atabaki et al. performed 85 ns reconfiguration of 4 um diameter microdisk, which is a factor of ten faster than traditional microheaters [40].

2.9 *Microheater IX*

Sherwood-Droz et al. have studied non-blocking optical 4x4 routers for Optical Networks on Chip (NoC) for future integrated photonic interconnection networks [49]. In single-wavelength networks, contention issues are experienced because multiple signals cannot overlap on the same optical cable. Therefore, Sherwood-Droz et al. designed a non-blocking hitless router [49]. Routing device is made up of eight mirrored resonators arranged to allow for efficient and unblocked internal routing, which can be seen in Figure 2.17. The width of the waveguides was set at 450 nm and the thickness as 250 nm. Sherwood-Droz et al. designed omega-shaped microheaters made of NiCr with a cross-sectional area of 1 µm x 0.1 µm with 10 µm radius and placed them 1 µm above the microrings [49]. The size of the device was 0.07 mm^2.

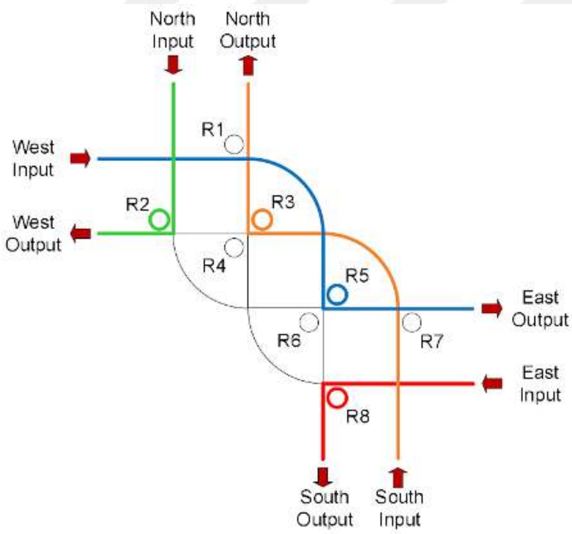

Figure 2.17: Designed 4x4 routing device [49].

For the input, a tunable continuous-wave laser was used at 1553.67 nm. As can be seen in more detail in Table 2.2, the FSR of the rings was obtained as 8.8 nm and the wavelength tuning efficiency was calculated as 0.25 nm/mW [49].

Performance Metrics: Sherwood-Droz et al. achieved 0.25 nm/mW switching power value [49].

Main Claimed Novelty: Sherwood-Droz et al. designed a 4x4 hitless router. This means that any of the available inputs may be routed to any of the available outputs without having to take the same physical path [49].

Table 2.2: Performances of the best-in-class microheaters.

Microheater	**References**	**FSR (nm)**	**Tuning Power per one FSR shift (mW)**	**Tuning Efficiency (mW/nm)**	**Wavelength Tuning Efficiency (nm/mW)**
I	Gan et al. [43]	16	56	3.50	*0.285
II	Geng et al. [44]	17	*105	6.187	*0.162
III	Dong et al. [45]	19	20.9	1.10	*0.909
IV	Dong et al. [46]	11.5	2.4	*0.21	4.76
V	Fang et al. [47]	12.9	4.9	0.38	*2.63
VI	Kim et al. [48]	35.37	29.2	*0.825	1.21
VII	Atabaki et al. [42]	*8.9	32	3.6	*0.27
VIII	Atabaki et al. [40]	*51	24.5	0.48	2.06
IX	Sherwood-Droz et al. [49]	8.8	*35.2	*4	0.25

*calculated

Chapter 3:
DESIGN, SIMULATION AND FABRICATION

This chapter begins by describing the purpose of the study in this thesis. Then, simulations were presented, and simulation results were compared to determine an efficient microheater geometry. After an efficient geometry is selected, the simulations made during the optimization of the features of specified structure are presented and the results obtained are compared. After determining the microheater's properties, heater's electrical and thermal properties are examined. Then, conversion of the structures into a suitable format for production is explained. This chapter concludes with a brief explanation of the production process of the designed microheater at Interuniversity Microelectronics Centre (IMEC) facilities.

3.1 Purpose

In the project, the microheater's purpose is to change the cut-off wavelengths by heating the silicon photonic filters located under the microheater from a certain distance. The most crucial issue to be considered here is how efficiently the designed heater works. Therefore, this thesis aims to design a microheater that consumes a minimum amount of power and increases the temperature of the device at the maximum rate. In other words, maximizing the amount of temperature that can be increased with a unit of power consumption.

3.2 Simulations

In the project, the microheaters to be designed will be located above the filters, and microheaters are produced by the Belgian company IMEC. For this reason, the type and dimensions of the materials used in the simulations were determined according to the rules specified by the company where the microheater and devices will be produced. Under these pre-determined rules, microheater design simulations were made in commercial software, COMSOL Multiphysics program. We chose COMSOL Multiphysics as our simulation environment, since it provides convenience in Joule heating simulations and heat transfer applications.

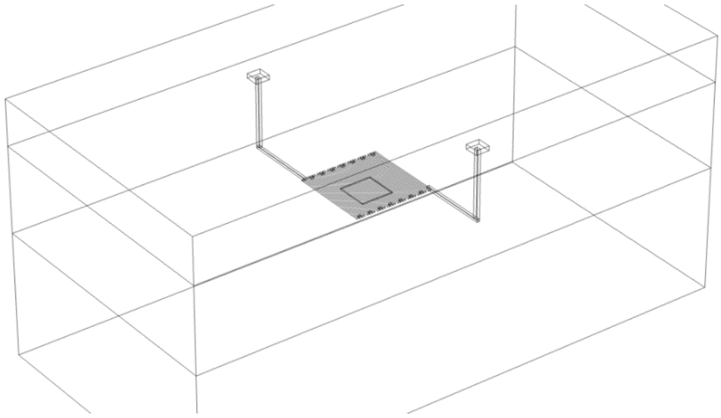

Figure 3.1: Microheater simulation environment in COMSOL Multiphysics.

Since the microheater designed here will be used in a real-life laboratory environment, a standard laboratory environment was created in COMSOL. As seen in Figure 3.1, the simulation region consists of three different layers, and the figure illustrates an example 3D simulation environment. The critical simulation circumstances due to fabrication rules and computer memory are summarized below:

1) The thickness of the actual substrate layer is 725 µm. Due to the computer's memory size, substrate thickness was reduced to 27 µm.
2) Since substrate is connected to the platform, substrate's bottom temperature was fixed to 293.15 K.
3) Thermal insulation is applied to each side of the simulation region, except the bottom region, because the temperature change in those areas is minimal.
4) Since the cladding is air, natural air convection was applied to the cladding layer.
5) According to the rules, the microheater material was chosen as W. The thickness and the width of the microheater were determined as 300 nm and 600 nm, respectively.
6) The microheater was positioned 1 µm above the device to be heated. The reason for this circumstance is to minimize absorption loss due to the microheater.
7) According to the rules, material of the interconnects was chosen as copper (Cu) because the resistivity of Cu ($1.712 \times 10^{-8}\Omega\text{m}$) [21] is less than W ($5.6 \times 10^{-8}\Omega\text{m}$), so most of the dissipation will happen in microheater. The thickness of the interconnects, which are connecting the microheater to the Cu pads, was chosen as 500 nm and the width as 600 nm.

3.2.1 The Geometry of the Microheater

The first thing to decide was what should be the shape of the microheater, so microheaters with three different designs were simulated in the COMSOL Multiphysics. These geometries were linear, parallel, and serpentine, and those heater simulations were done for two different target temperature values. Figure 3.2 shows the simulated microheater designs.

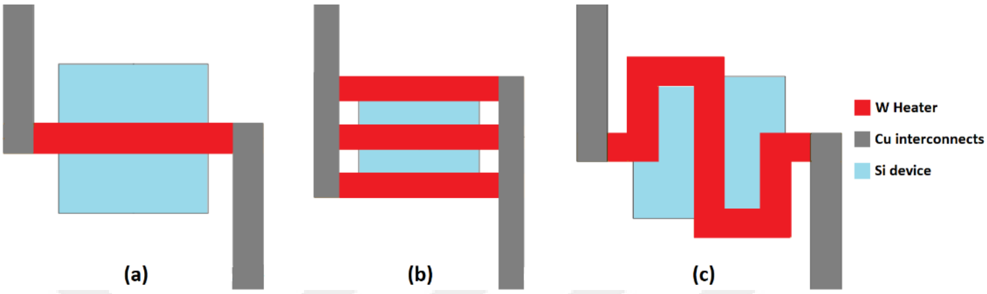

Figure 3.2: (a) Linear microheater, (b) parallel microheater, (c) serpentine microheater.

In these simulations, the ambient temperature of the device was set to 293.15 K. In the first simulation, the maximum temperature on the device was aimed to be 307 K. In the studies reported in the literature, it has been observed that the temperature of the microheaters placed 1-2 μm above the device is increased between 100-150°K on the device to provide the necessary phase shift. Since our microheaters were placed 1 μm above our filters, a temperature increase of 100°K was aimed on the device in the second simulation. As a result of these simulations, values such as the amount of power consumed by the microheater systems in these simulations, the temperature difference on the device, the amount of current passing through the microheater were recorded in the table for comparison. Potential difference between pads represents the created potential difference between the conductive pads of the microheater system. The current column shows the current passing through the microheater. Maximum and minimum temperature values show the highest and lowest temperature values on the heated device. The difference between these two values shows the temperature difference on the device, which gives an opinion about the temperature uniformity on the heated structure, and temperature uniformity factor has a significant role in the performance comparison of the microheaters. Finally, the power column shows the power consumption of the heater system, which is another crucial factor for microheater performance comparison. The power consumed by the heater system is given by the equation:

$$P = IV = \frac{V^2}{R} \tag{3.1}$$

In this equation, V is the voltage applied to the heater system, I is the current passing through to the system, and R is the resistance of the heater system.

Table 3.1: Simulation results of the different shapes of microheaters when the maximum device temperature is 307 K.

Geometry	Pot. Diff. Between Pads (V)	Current (mA)	Max. Temp. (K)	Min. Temp. (K)	Temp. Diff. (K)	Power (mW)
Linear	0.100	27.3	307.02	306.39	0.63	2.7300
Parallel	0.094	35.2	307.00	306.69	0.31	3.3088
Serpentine	0.100	20.2	307.23	306.56	0.67	2.0200

Table 3.2: Simulation results of the different shapes of microheaters when the maximum device temperature is 393 K.

Geometry	Pot. Diff. Between Pads (V)	Current (mA)	Max. Temp. (K)	Min. Temp. (K)	Temp. Diff. (K)	Power (mW)
Linear	0.2690	73.50	393.538	388.98	4.558	19.771
Parallel	0.2545	135.80	393.000	391.50	2.500	34.560
Serpentine	0.2670	53.84	393.347	389.00	4.347	14.380

Performance comparisons were made mainly on the temperature differences in the Si device and the power consumption of each microheater type. Figure 3.3 illustrates the results of the simulated microheater geometries when the maximum temperature on the device is around 393 K.

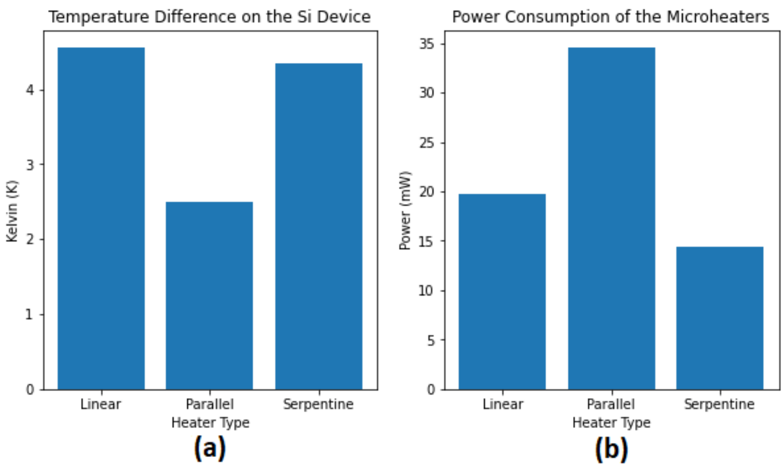

Figure 3.3: Performance results: (a) temperature difference on the Si device, (b) power consumption.

When the simulation results are examined, the minimum temperature difference is seen on the device, which is heated by using a parallel heater. On the other hand, the minimum power consumption was calculated on the system, which has a serpentine-shaped heater. According to the power consumption results in Figure 3.3, the system with the parallel heater consumed 140% more power than the system with the serpentine heater, and the system with the linear heater spent 37.5% more energy than the system with the serpentine-shaped heater. In addition, when the ambient temperature profiles of the simulations were examined, it was observed that heat dissipation occurred in all parts of the microheater system with a parallel heater. In the same way, linear heater also heated the environment in which linear heater is located but not as much as a system with the parallel heater. Because of the low resistance of linear and parallel microheaters, heat dissipation occurred in the Cu interconnects and conductive pads and this dissipation caused high power consumption. On the other hand, when the figure below is examined, it is seen that the heat emitted by the serpentine-shaped heater is around the heater region and serpentine heater's heat emitting profile is better than the linear and parallel heater. The YZ thermal profiles of the linear, parallel, and serpentine-shaped heater at the same target temperature value on the heated device are illustrated in Figure 3.4.

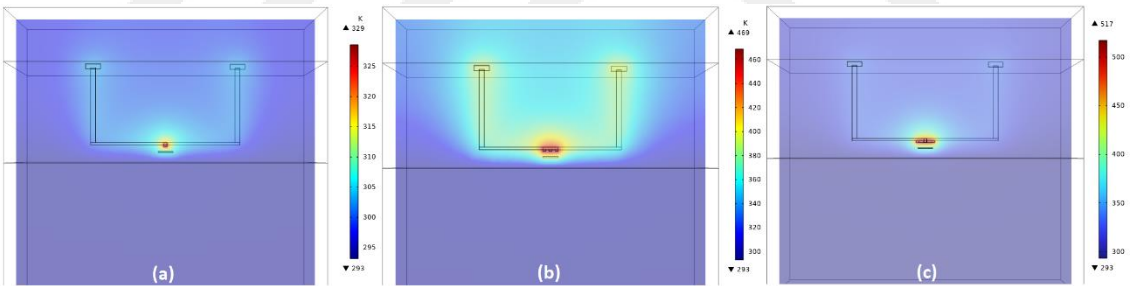

Figure 3.4: Temperature profile of (a) linear heater, (b) parallel heater (c) serpentine-shaped heater.

After comparing the obtained results, the best shape of the heater was decided on as a serpentine. After determining the microheater shape, the optimization of the serpentine heater properties was divided into two parts. The first step was the optimization of the distance between the grids of the serpentine-shaped heater. The second part was determining the amount of the microheater overflow on the device. The parts to be optimized on the microheater design are shown in Figure 3.5. In Figure 3.5, d represents the space between each grid, and L represents the overflow of the microheater over the Si device.

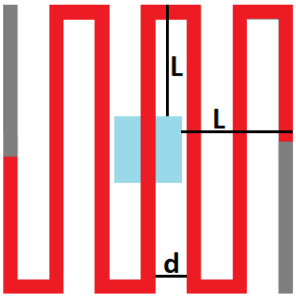

Figure 3.5: Display of spacing between microheater lines (d) and overflow (L).

3.2.2 Separation Between the Microheater Lines

The first part of the optimization process is the optimization of the spacing between the microheater lines of the serpentine-shaped heater. According to the production rules, the minimum distance between the heater grids must be at least 0.6 µm. Considering this rule, simulations were made at three different distance values, which were 0.6 µm, 0.8 µm, and 1 µm. These designs are illustrated in Figure 3.6. In these simulations, heated devices are of different sizes, and the amount of overflow of the microheater on the device is kept the same. Horizontal and vertical overflows were set as 4 µm and 4.6 µm, respectively. Acquired data were processed into the table when the maximum temperature on the device is around 393 K. Table 3.3 shows obtained results from these simulations.

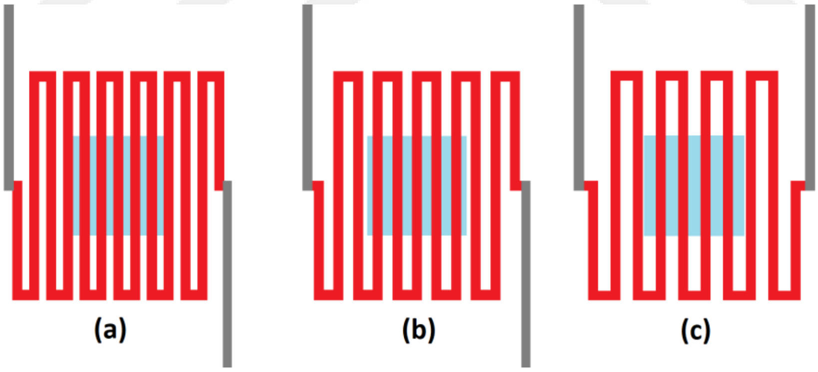

Figure 3.6: Simulated microheater designs with different spacing value: (a) d=0.6 µm, (b) d=0.8 µm, (c) d=1.0 µm.

Table 3.3: Simulation results of the microheaters with different spacing values.

Spacing (µm)	**Pot. Diff. Bet. Pads (V)**	**Current (mA)**	**Max. Temp. (K)**	**Min. Temp. (K)**	**Temp. Diff. (K)**	**Power (mW)**
0.6	1.270	22.489	393.418	391.726	1.692	28.557
0.8	1.360	28.167	393.096	391.354	1.742	38.307
1.0	1.328	29.974	393.974	392.022	1.952	39.805

Performance comparisons were made mainly on the temperature uniformity in the Si device and the power consumption of each microheater with different separation values between heater lines. Figure 3.7 demonstrates the results of the simulated microheaters.

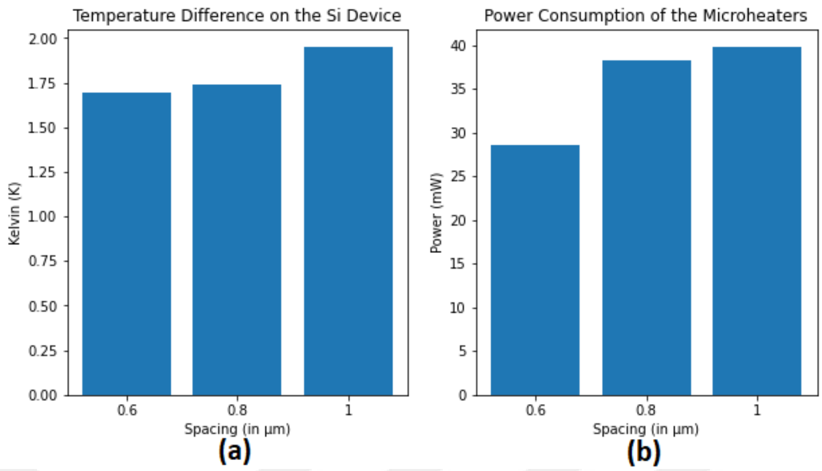

Figure 3.7: Performance results: (a) temperature difference on the Si device, (b) power consumption.

As seen in Figure 3.7, we observed that the temperature difference on the heated device increased as the space between the grids of the serpentine microheater expanded. These results show enlarging the separation between the heater lines decreases the temperature homogeneity on the heated device. When the power consumption of microheater systems is calculated, we have seen that the amount of power consumed by the system increases as the distance between the heater rods increases. As the distance between the heater rods increased, the number of grids in the heater decreased, which caused the resistance of the microheater to decrease. We calculated the heater with the lowest power consumption was the one with 0.6 µm gap value. The microheater with 1.0 µm spacing consumed 39.4% more power than the microheater with 0.6 µm separation. Moreover, the microheater with 0.6 µm spacing between microheater lines consumed 34% less power than the microheater with 0.8 µm spacing between microheater lines. As a result, considering the low power consumption and temperature uniformity performance, the distance between the microheater grids was determined as 0.6 µm.

3.2.3 Overflow Amount Over the Device

After specifying the most suitable separation value between microheater lines, how much the heater will overflow over the device was decided with the simulations made. These simulations were made on a sample device with a length of 7 µm and a width of 7 µm.

The data obtained were processed into the table around 393 K, the maximum temperature on the device. These designs are illustrated in Figure 3.8. Table 3.4 shows obtained results from these simulations.

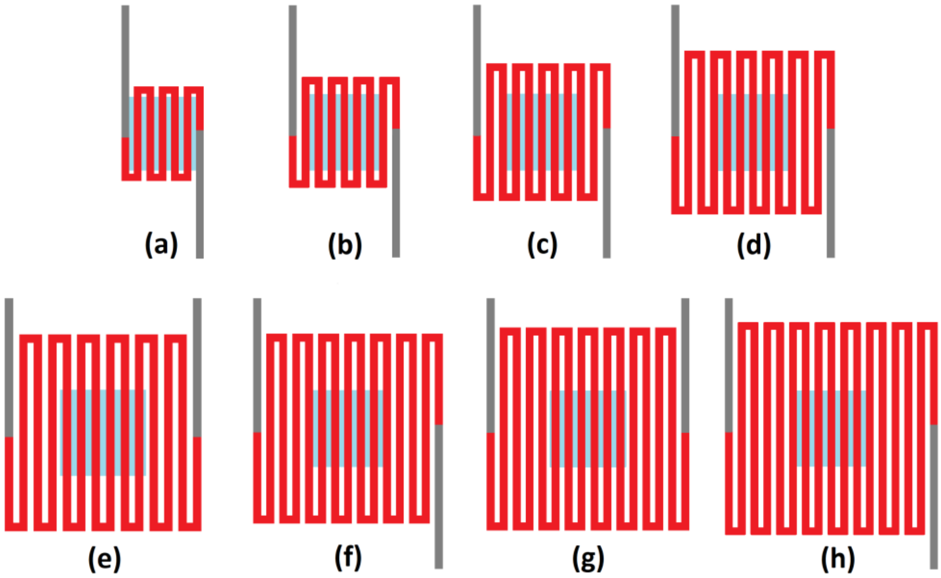

Figure 3.8: Simulated microheater designs with different overflow values: (a) L=0.4 µm, (b) L=1.6 µm, (c) L=2.8 µm, (d) L=4 µm, (e) L=4.6 µm, (f) L=5.2 µm, (g) L=5.8 µm, (h) L=6.4 µm.

Table 3.4: Simulation results of the microheaters with different overflow values.

Overflow	**Pot. Diff. Bet. Pads (V)**	**Current (mA)**	**Max. Temp. (K)**	**Min. Temp. (K)**	**Temp. Diff. (K)**	**Power (mW)**
0.4 µm	0.50	32.45	393.650	383.620	10.03	16.225
1.6 µm	0.68	27.11	392.615	387.392	5.223	18.43
2.8 µm	0.92	24.59	394.364	391.187	3.177	22.62
4.0 µm	1.20	22.90	394.403	392.564	1.839	27.48
4.6 µm	1.35	21.87	393.430	391.960	1.470	29.53
5.2 µm	1.51	21.55	392.670	391.400	1.270	32.54
5.8 µm	2.02	25.27	393.330	392.310	1.020	51.05
6.4 µm	2.26	25.00	393.360	392.530	0.830	56.50

Performance comparisons were made mainly on the temperature differences in the Si device and the power consumption of each microheater with different overflow amounts. Figure 3.9 shows the results of the simulated microheaters.

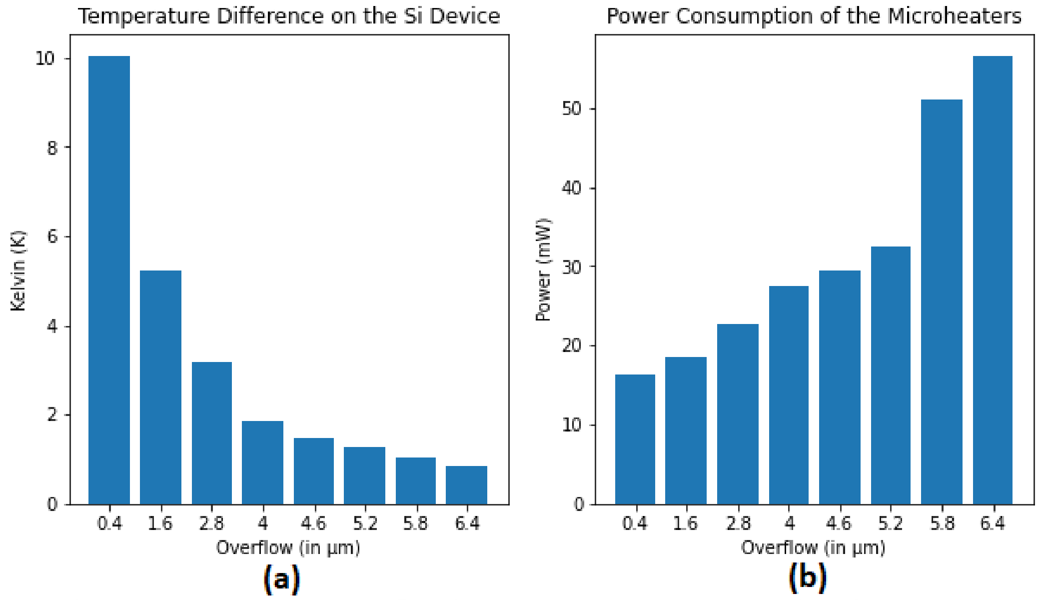

Figure 3.9: Performance results: (a) temperature difference on the Si device, (b) power consumption.

When the results were examined, it was seen that when the overflow amount of the heater on the device was expanded, the temperature difference on the device dropped. On the other hand, the microheater resistance increased with the amount of overflow, and more volts were needed for sufficient temperature rise. Since the consumed power of the heater is V^2 dependent, the amount of power consumed by the system increased. To make a more comfortable elimination, the temperature difference of 2 K is accepted as the threshold. Microheaters with an overflow of 0.4 µm, 1.6 µm, and 2.8 µm were eliminated because temperature difference on the heated device was greater than the threshold value. In order to make more sifting between the remaining heaters, the power consumption and temperature differences of the heaters were examined. Microheaters with 6.4 µm and 5.8 µm overflows were eliminated as they consumed approximately 30%-40% more power than the other microheaters. As a result of the comparison between the remaining, the best overflow amount was determined to be 5.2 µm because the minimum temperature difference on the device was seen in these heater simulations.

After finding the optimum overflow and separation values, it was decided where and how to make the connection between the interconnects and the resistive layer. In these simulations, the designed microheater is connected to copper interconnects with three different styles and from three different locations. Figure 3.10 shows these different connection styles between the Cu connections and the microheater.

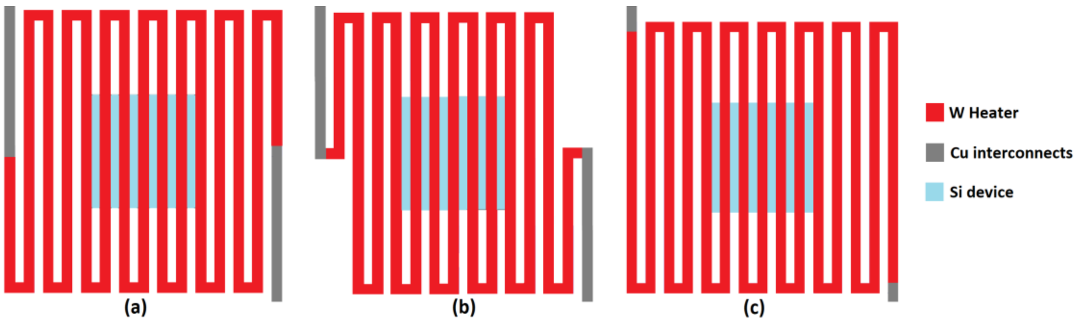

Figure 3.10: Different versions of microheater-copper connections (a) version 1, (b) version 2, (c) version 3.

In the first version, copper rods are attached to the ends of microheater and these tips are located at the center of both sides of the microheater. In the second version, the resistance of the system is increased by making additional short additions to the ends of the heater. In the last version, the ends of the heater are elongated, and the copper connections are connected to the heater system from the edge.

Table 3.5: Simulation results of the microheaters with different connection versions.

Type	**Input Volt. (V)**	**Current (mA)**	**Max. Temp. (K)**	**Min. Temp. (K)**	**Temp. Diff. (K)**	**Power (mW)**
Version 1	1.51	21.55	392.685	391.510	1.175	32.54
Version 2	1.35	22.17	393.392	391.662	1.730	29.93
Version 3	1.60	21.41	393.014	391.948	1.066	34.26

Simulations were done using a microheater with a 0.6 µm spacing between heater lines and a 5.2 µm overflow. During these simulations, the temperature above a device with a length and width of 7 µm was requested to be 393 K. When the obtained results were compared, it was seen that the temperature difference on the device heated by using the 3rd version heater decreased significantly. When the power consumption was compared, it was seen that the 3rd version heater consumed 5.3% more power than the 1st version heater. However, this difference was ignored, and the attachment method specified in version 3 was chosen as the most appropriate for the heater system.

The final configuration of the microheater is a serpentine shape, with a cross-sectional area of 0.6x0.3 µm^2. The distance between the grids of the serpentine-shaped heater was determined as 0.6 µm, and the amount of overflow of the microheater over the device was specified as 5.2 µm. The designed microheater's electrical and thermal simulation analysis is examined in the following section.

3.3 *Electrical and Thermal Analysis of the Designed Microheater*

After specifying the necessary features of the designed microheater, the electrical and thermal properties of this microheater were examined. In addition, the effect of the temperature change on the effective index of the device was investigated. Before starting simulations, since substrate is connected to the platform, the temperature of the bottom side of the simulation region is set to 293.15 K. Except for this bottom region, thermal insulation has been applied to each side of simulation region. A 7 µm long and 7 µm wide device was placed 1 µm below the microheater, and the initial temperature of this device was set to 293.15 K. To obtain an accurate thermal efficiency, 9 different potential differences were applied between the contact pads which means 9 different simulations were made. In each simulation, potential difference between microheater ends, current passing through microheater, and average temperature value obtained on the device was measured, average temperature increase on the device and the power consumed by the microheater to obtain this temperature value was calculated. Table 3.6 illustrates the values obtained from these simulations.

Table 3.6: Simulation results of the microheaters with different potential difference values between pads.

Pot. Diff. Bet. Pads (V)	**Pot. Diff. Bet. Microheater Ends (V)**	**Current (mA)**	**Average Temp. (K)**	**Average Temp. Inc. (K)**	**Power (mW)**
0.6	0.5800	8.03	303.057	9.907	4.660
0.7	0.6800	9.37	306.635	13.485	6.340
0.8	0.7740	10.70	311.120	17.970	8.278
0.9	0.8700	12.04	315.890	22.740	10.480
1.0	0.9670	13.378	320.630	27.480	12.938
1.1	1.0638	14.716	326.400	33.250	15.656
1.2	1.1605	16.054	332.720	39.570	18.631
1.3	1.2570	17.392	339.590	46.440	21.866
1.4	1.3540	18.730	346.997	53.847	25.360

To find the resistance of the microheater, linear regression was applied to the potential difference on the microheater and current passing through microheater. Figure 3.11 shows the potential difference versus the current graph of the microheater. It is seen that the current passing through the heater increases as the potential difference between the microheater ends increases. Moreover, we can say the conductor exhibits ohmic behavior because the data increases linearly. As a result of linear regression, the resistance of the microheater was calculated as 72.1 Ω.

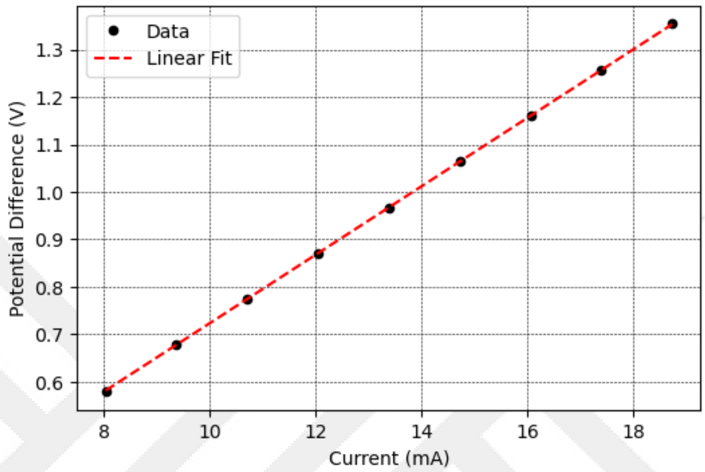

Figure 3.11: Potential difference versus current graph of our microheater.

After obtaining values in Table 3.6, a linear regression was applied to the average temperature increase on the device and the amount of power consumed for this temperature increase in order to calculate thermal efficiency of our heater. As a result of linear regression, the thermal efficiency of our microheater was calculated as 2.115 K/mW. Figure 3.12 illustrates the relation between power consumption of the microheater and the average temperature change on heated device.

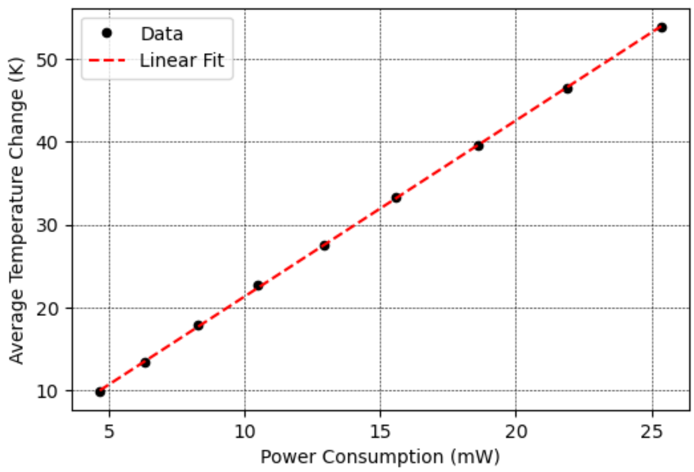

Figure 3.12: Average temperature change on the Si device for different power consumptions.

In addition to electrical and thermal properties, the heat emitted from the microheater and the consequence of temperature change on the effective index of the device were analyzed. Heat dissipation of a resistor can be determined by the following equation:

$$Q = I^2 R \Delta t \quad (3.2)$$

In Equation (3.2), I is the current passing through the resistor, R is the resistance of the resistor and Δt represents time interval. As can be seen from the equation, there is a direct proportionality between the current passing through the resistor, the resistance value and the time change and the heat dissipated from the microheater. While calculating the heat dissipated from the microheater in each simulation, the resistance value calculated in the electrical analysis section and the current values measured in Table 3.6 were used. Table 3.7 shows dissipated heat from microheater in each simulation.

Table 3.7: Dissipated heat from microheater in each potential difference.

Pot. Diff. Bet. Pads (V)	**Current (mA)**	**Resistance (Ω)**	**Time Interval (µs)**	**Dissipated Heat (µJ)**
0.6	8.03	~72.1	~15	8.685
0.7	9.37	~72.1	~15	10.133
0.8	10.70	~72.1	~15	11.572
0.9	12.04	~72.1	~15	13.021
1.0	13.378	~72.1	~15	14.468
1.1	14.716	~72.1	~15	15.915
1.2	16.054	~72.1	~15	17.362
1.3	17.392	~72.1	~15	18.810
1.4	18.730	~72.1	~15	20.257

As can be seen from the results obtained, the amount of heat emitted from the heater increased as the amount of current passing over the microheater increased. In addition, it was observed in the simulations that the devices reached maximum temperatures in approximately 15 µs. This is because the heater is placed 1 µm above the device, and there is a SiO_2 layer with low thermal conductivity between them. The effective index change of the waveguide material due to temperature change is determined by the following equation:

$$n_{eff} = n_{eff,25°C} + \left(\frac{dn_{eff}}{dT}\right) \Delta T \quad (3.3)$$

In Equation (3.3), $n_{eff,25°C}$ is the effective index of the waveguide material at room temperature, $\frac{dn_{eff}}{dT}$ is the thermo-optic coefficient of the material, and ΔT is temperature change. At 293.15 K, silicon's effective index is around 3.48 and silicon's thermo-optic coefficient is $1.86 \times 10^{-4} K^{-1}$. By using these values and average temperature increase on the device values in Table 3.6, we calculated effective index change of the device. As can be seen from the results obtained, the effective index of silicon increased as the temperature change on the device increased.

Table 3.8: Effective index change of the device in each simulation.

Pot. Diff. Bet. Pads (V)	Average Temp. Increase (K)	New Effective Index
0.6	9.907	3.4818
0.7	13.485	3.4825
0.8	17.970	3.4833
0.9	22.740	3.4842
1.0	27.480	3.4851
1.1	33.250	3.4861
1.2	39.570	3.4874
1.3	46.440	3.4886
1.4	53.847	3.4900

3.4 Conversion of the Microheater Design into GDSII Form

Before the fabrication step of the designed microheaters, these microheaters must be added to the mask. The masks to be sent to production are sent in a particular format, a GDSII file. The microheaters sent to production are designed with an algorithm written using the Gdspy library, a free library in the python programming language. Since the dimensions of the microheaters will differ according to the sizes of the devices to be heated, their sizes are chosen according to the device sizes entered by the user in the written algorithm. In addition, the length and width of the copper interconnects used, and the length of the connector placed between these connections and the pad are left to the user. In this way, user can determine the area covered by the whole system as the user wishes.

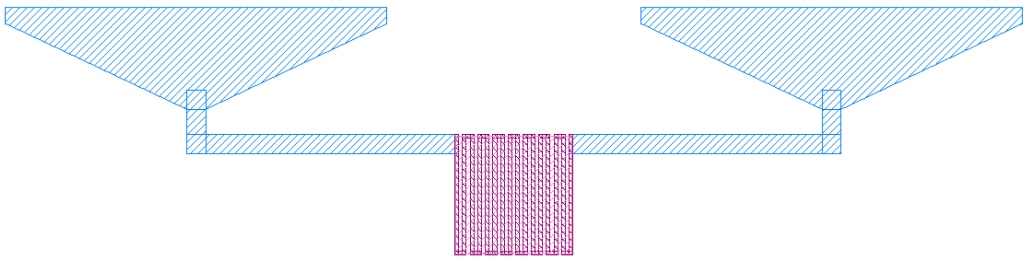

Figure 3.13: An example microheater system in GDSII format.

The figure above shows an example microheater system. The blue-colored objects in this system show the copper objects. The hexagonal coppers or pad connectors located at the ends of the copper rods are designed as the slots of the pads. Copper pads are added to these slots before the designed heater is placed in the mask in the last step. The designed heater and device were centered between the pads, and the distance between these pads was set as 40 µm. To add our designs to the mask before sending mask to fabrication, we transferred our designs to the mask with IMEC's own Process Design Kit (PDK), IMEC iSiPP50G. An example microheater system attached to the mask for production can be seen in Figure 3.14.

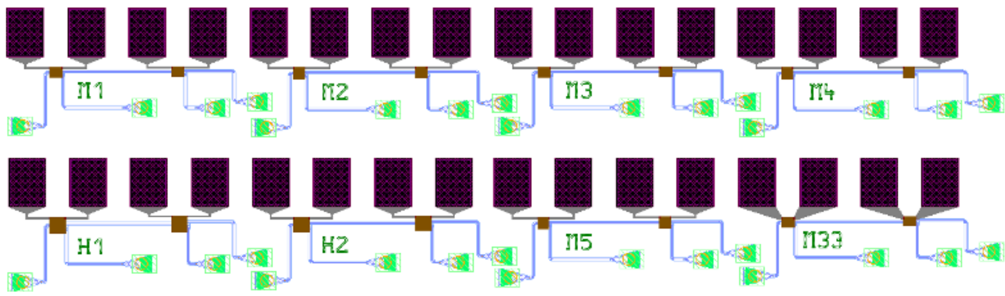

Figure 3.14: Sample microheater systems placed on the mask.

3.5 *Fabrication*

Our devices and microheaters were fabricated in the IMEC factory. In this fabrication process, first of all, the designed devices and heaters are written with a laser on two separate chrome plates, for devices and heaters, and these plates are used as a mask. With the photolithography method, device designs are transferred on the plate covered with a photoresist layer. Then, the parts exposed to the light are dissolved by the washing process. The silicon layer under the photoresist material remaining with the scraping process is scraped to a certain thickness. With the PECVD method, the remaining parts of the silicon layer are covered with 2 µm SiO2. Before starting the fabrication of the microheaters, firstly, the top of the wafer is cleaned with special solutions. Then, with a pre-baking method, the cleaning solution on the wafer is evaporated for better adhesion of the photoresist. Later, the wafer is put into a hopper. Here wafer is rotated and covered with photoresist material. The purpose of rotation in this step is to ensure that the photoresist material is spread evenly on the surface. Finally, the wafer is heated in the soft baking method, and the photoresist material on it dries and sticks. Again, the heater designs are transferred onto the photoresist layer by photolithography, and then washed with solvent. This washing process is called as development. The surface of the plate, with the remaining photoresist material on it, is covered with metal using one of the physical vapor deposition methods (evaporation or sputtering [3]). Finally, the metal layer is shaped by the lift-off method. In this technique, the wafer is submerged into a particular solution, and the solution is reacted with a photoresist layer. Because of this reaction, the solvent lifts off the metal which is contacted with the photoresist layer, and this technique is called lift-off. Finally, the designed microheaters are formed on the layer. The microheater fabrication process is illustrated in Figure 3.15.

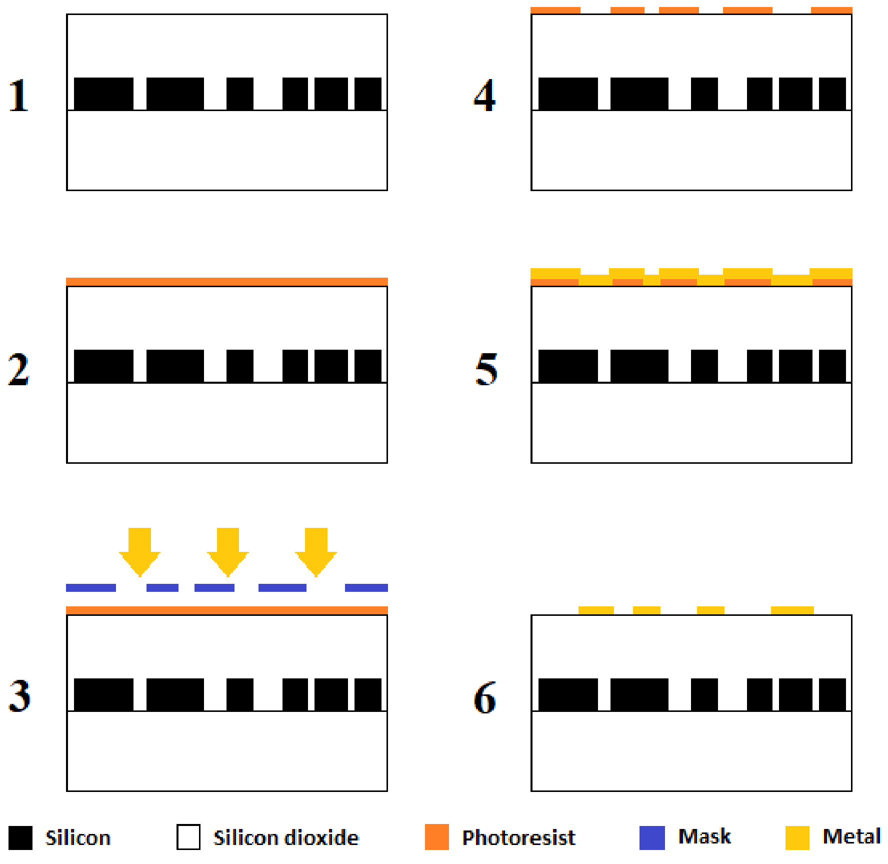

Figure 3.15: An example fabrication process of microheater in IMEC.

Chapter 4:
DISCUSSION

This chapter provides the performance results of our designed microheater and compares our microheater's performance result with the performances of the best-in-class microheaters in the photonics presented in Chapter 2. Then, it focuses on the reasons for the performance differences and describes them.

4.1 *Thermal Efficiency of the Designed Microheater*

As mentioned in Chapter 3.3, nine different potential differences were created between the pads of the microheater. In these simulations, initial temperature of the Si device was set to 293.15 K. The average temperature increase on the device and the amount of power consumed for this temperature increase were obtained from these simulations. After applying linear regression to the obtained values, the slope of the obtained line gave us the thermal efficiency value. As a result of linear regression, the thermal efficiency of our microheater was calculated as 2.115 K/mW. From this thermal efficiency result, we can deduce that, the microheater we designed should consume 4.73×10^{-1} mW for 1 K temperature change.

4.2 *Thermal Efficiencies of the Best-In-Class Microheaters*

As mentioned in Chapter 2, using the thermo-optic effect is a frequent method in the reconfiguration of Si photonic devices. Using the thermo-optic effect, the phase of the light passing through the waveguide can be changed. This phase change is achieved by changing the effective index of the waveguide material. As mentioned in Chapter 3.3, the effective index change of the waveguide material due to temperature change is determined with Equation (3.3). Phase of the waveguide can be defined as

$$\phi = \frac{2\pi}{\lambda} n_{eff} L \tag{4.1}$$

In Equation (4.1), λ is the input wavelength of the waveguide, n_{eff} is effective index of the waveguide material, and L is length of the waveguide. From Equation (3.3) and (4.1) we can get the following equation.

$$\Delta\phi = \frac{2\pi}{\lambda} L \left(\frac{dn_{eff}}{dT}\right) \Delta T \tag{4.2}$$

Equation (4.2) gives the effect of the temperature change on the phase change of a waveguide. According to the Dong et al., for tuning one FSR of a ring resonator, 2π phase change is required [45]. Using Equation (4.2), we calculated the thermal efficiencies of the best-in-class microheaters mentioned in Chapter 2. In these calculations, for λ we used the input wavelength specified in these studies, for $\frac{dn_{eff}}{dT}$ used thermo-optic coefficient of Si, and for L used the perimeter of a ring resonator. Table 4.1 shows the thermal efficiency and power consumption for 1 K temperature change of our design and best-in-class microheaters. Table 4.1 also provide characteristics of the heaters, which is another crucial factor on the performance of the microheater. In Table 4.1, Device & Heater Contact column shows the connection between heater and device. Gap means there is a SiO_2 layer between these two structures and direct represents the direct connection between the heater and the device. Heat insulation column shows whether thermal insulation is provided in the system with the trenches. Finally, microheater material column gives information about heater material.

Table 4.1: Performances and characteristics of the microheaters.

Microheater	**References**	**Thermal Eff. (K/mW)**	**Power Cons. (x 10^{-2}) (mW/K)**	**Heater Material**	**Device & Heater Contact**	**Heat Isolation**
IV	Dong et al. [46]	73.24	1.36	Ti	Gap	Isolation trench
V	Fang et al. [47]	34.36	2.91	NiSi	Direct	Isolation trench
VIII	Atabaki et al. [40]	27.067	3.69	NiCr	Direct	No trench
VI	Kim et al. [48]	18	5.56	Cr	Gap	No trench
III	Dong et al. [45]	13.642	7.33	Ti	Gap	Isolation trench
VII	Atabaki et al. [42]	4.145	24.1	Ni	Gap	No trench

IX	Sherwood-Droz et al. [49]	3.777	26.5	NiCr	Gap	No trench
I	Gan et al. [43]	3.375	29.6	Ti	Gap	No trench
II	Geng et al. [44]	2.515	39.2	Ti	Gap	No trench
	Our Microheater	2.115	47.3	W	Gap	No trench

4.3 Comparison of Our Design with Best-In-Class Microheaters

As can be seen from Table 4.1, Fang et al. [47] and Dong et al. [46] microheater structures are far more efficient than our design and other best-in-class microheater designs because of the air isolation trench or undercut beneath the waveguide that Fang et al. [47] and Dong et al. [46] used in their microheater structure. Fang et al. [47] and Dong et al. [46] got such good results because of the air isolation trench that they created by etching the substrate layer because, in a microheater system, the primary heat sink is the Si substrate layer [46]. Also, isolation trench prevented the heat from spreading to the adjacent SiO_2 layer, reduced heat loss through the membrane, and focused the heat on the ring resonator. The effect of air isolation trench on power consumption is also seen in the published studies of this structure. As mentioned in Chapter 2, Fang et al. studied two different designs to see the effect of the air isolation trench on the efficiency of the microheater [47]. One design has air isolation trench, while the other design does not have this isolation trench. According to obtained results of Fang et al., the design with an air isolation trench was 92% more efficient than the other design [47].

The position of a microheater affects heater's efficiency. Fang et al. formed their NiSi microheater on both sides of the ring resonator on the Si slab region [47]. The generated heat from the microheater was transferred straightly to the ring resonator. This direct connection and sandwiching of the ring resonator with microheaters improved temperature rise response, and significantly reduced the power consumption of the microheater. Atabaki et al. positioned their microheater directly on the microdisk [40]. With this direct connection, Atabaki et al. prevented the heat from spreading to the BOX layer, and ensured that generated heat was transferred directly to the waveguide [40]. On the other hand, we placed our microheater 1 μm above the Si device because of the fabrication rules. That's why the heat emitted from our design had to transfer through the BOX layer. In addition, since the thermal conductivity of the SiO_2 (0.014 W/cm K) is much less than Si (1.35 W/cm K) [46], our design had to consume more power.

The difference in materials used in the microheater's design also affected the heater's performance. Resistivity of the resistive layer materials in best-in-class microheaters is higher than the resistivity of W. The resistivity of NiSi is around $13 - 14 \times 10^{-8}\Omega$m [50], at 20°C, the resistivity of NiCr is approximately $110 \times 10^{-8}\Omega$m, [3] and the resistivity values of other used materials in these studies are given in Table 1.1 in Chapter 1. Using material with high resistivity for best-in-class microheaters has been influential in the performance of the best-in-class microheater designs. To see the effect of using a material with higher resistivity than tungsten, we changed our microheater material to chromium and calculated the thermal efficiency of that microheater. We used the same microheater structure and simulation environment as we used in Section 3.3. Again, nine different potential differences between conductive pads were created, and the average temperature rise on the device and power consumption for that average temperature rise was calculated. Then, we applied linear regression to these results. As a result of linear regression, the thermal efficiency of Cr microheater was calculated as 3.057 K/mW. Figure 4.1 illustrates the relation between power consumption of the microheater and the average temperature change on heated device.

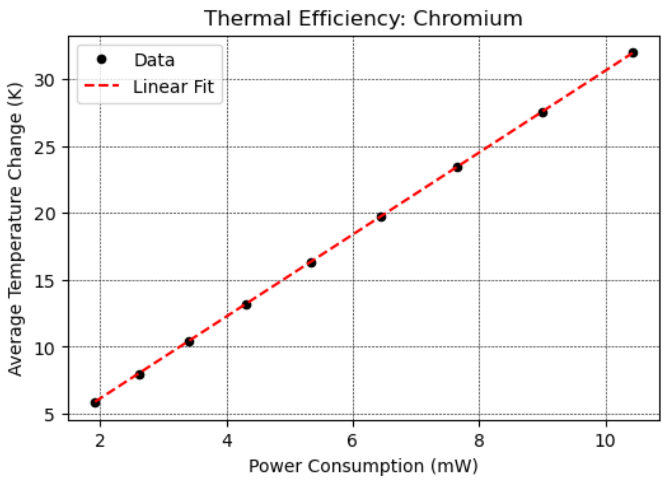

Figure 4.1: Average temperature change on device versus power consumption of chromium microheater.

4.4 *Effect of Our Optimizations on the Microheater Efficiency*

In addition to the microheater's placement and material, the microheater's geometry and the characteristics of heater design also significantly affected the performance. We decided on the serpentine-shaped microheater because, in the simulations we have made on the heater geometry, it has been observed that the heater with a serpentine shape consumes less power than other structures. The parallel heater showed better temperature uniformity on the Si device, but parallel heater consumed twice as much energy as the serpentine-shaped heater. In addition, when the thermal profiles of the three heaters are examined, it has been observed that the heat is not only formed on the microheater but also on the pad and connections in the linear heater system and parallel heater system. The conductive pads and contacts should not heat up significantly for an efficient, long-lasting microheater. Therefore, we chose serpentine shape as our microheater geometry. Furthermore, as mentioned in the Introduction section, previous studies reported that the meander or serpentine structure showed uniform temperature distribution while consuming low power [3], [25]–[27].

After specifying the microheater geometry, we focused on determining the characteristics of the serpentine-shaped heater because the overflow amount of the heater over the device and the separation between heater lines has a crucial influence on the temperature uniformity on the Si device. Firstly, we studied on choosing the efficient separation between heater lines. In these simulations, we observed that minimizing the separation between the microheater lines reduced the power consumption. Therefore, to increase the power efficiency of our design, we chose the separation value with the lowest power consumption. After choosing the proper distance value between the heater lines for our heater, we moved to the next step of our optimization, which is determining the overflow amount of the microheater over the Si device. In these simulations, we have seen that as the amount of overflow increases, the temperature difference on the device decreases. On the other hand, we observed an increase in the amount of power consumed as the resistance of the microheater increased as the amount of overflow increased. Here, we chose the one that provides high temperature homogeneity and does not consume excessive power. Finally, we determined the connection position of the microheater and the interconnects. In order to increase the temperature homogeneity on the device, we extended our heater from its ends. Extending microheater also had an effect on the efficiency of the heater.

Chapter 5:
CONCLUSION

This chapter summarizes the content of this thesis and briefly explains demonstrated results. Furthermore, future works related to this thesis are mentioned in the following section of this chapter.

5.1 Thesis Summary

In Chapter 2, studies using best-in-class microheaters used in photonics are described. The geometry, material type, connection type with the device, and air insulation of the microheaters used in each study were examined and this information was collected in Table 2.1. In addition, tuning power per one FSR shift, tuning efficiency, and wavelength tuning efficiency, which are important in the performance comparison of these microheaters, were obtained and collected in Table 2.2. When the performance results are examined, it is seen that the air insulation and the direct connection between the heater and the device increase the microheater efficiency.

In Chapter 3, firstly, simulations for determining the proper microheater geometry are made, and their results are examined. From those results, proper microheater geometry was determined as serpentine. Following the selection of suitable geometry, the simulations conducted to optimize its aspects were shown, and the resulting outcomes were contrasted. As a result of the simulations, the distance between the heater lines was specified as 0.6 μm, and the amount of overflow of the heater over the device was defined as 5.2 μm. After determining the required properties of the microheater, the electrical and thermal properties of the structure were examined. As a result of these studies, the thermal efficiency of the design was calculated as 2.115 K/mW. The following section described how to convert microheaters to GDSII format before being sent to production. In the final section of this chapter, the microheater production step is explained step by step.

In Chapter 4, our design is compared with best-in-class microheaters. These comparisons were made over the thermal efficiencies of the microheaters. The thermal efficiencies of the best-in-class microheaters were obtained by using the equation of phase change on the resonator depending on the temperature change. The obtained values were compared with the performance of our design and the reasons for the performance difference were examined. The reasons leading to the performance difference were determined as the air isolation trench in the system, the type of connection between the microheater and the device, and the material from which the microheater is made. From the results obtained, it has been seen that the designs with air isolation ditch are many times more efficient than our design. A similar performance difference was also observed when our design was compared with designs with a direct connection between the heater and the device. The reason for the performance difference with the remaining microheaters was the type of material used in the production of the microheater. To see the effect of the material with a higher resistivity value, the same simulations were done that we did to determine the performance of the tungsten microheater, changing the heater material to chromium. As a result of these simulations, it was seen that the performance of the Cr microheater was 44% better than the microheater made from W.

5.2 Future Works

Future works of this work include laboratory experiments and improving the performance of the microheater.

1) To carry out the experiments performed in the simulation environment in a real-life laboratory environment and obtain a consistent phase shift by heating the Si photonic filters.
2) The situations where electromigration will take place will be examined and necessary fault detections will be made.
3) Changing resistive layer material from tungsten to metals with higher resistivity values like platinum or chromium would reduce the power consumption of the microheater system.
4) Like the ones in the best-in-class microheaters adding trenches to the sides of the microheater or adding air isolation trenches beneath the Si device would increase the efficiency of our microheater.
5) Changing microheater geometry from serpentine/meander to more complex geometries or creative geometries like Sujatha et al. may improve the device's temperature uniformity and decrease the system's power consumption.

BIBLIOGRAPHY

[1] J. P. Joule, “XXXVIII. On the heat evolved by metallic conductors of electricity, and in the cells of a battery during electrolysis,” *Lond. Edinb. Dublin Philos. Mag. J. Sci.*, vol. 19, no. 124, pp. 260–277, Oct. 1841, doi: 10.1080/14786444108650416.

[2] S. Sohrabi, L. Hajshahvaladi, M. K. Moraveji, E. Sohrabi, and F. Heidarpoor, “Patterned synthesis of nanowires in microheaters: design and operational aspects,” *Microfluid. Nanofluidics*, vol. 26, no. 1, p. 3, Dec. 2021, doi: 10.1007/s10404-021-02506-y.

[3] Z. E. Jeroish, K. S. Bhuvaneshwari, F. Samsuri, and V. Narayanamurthy, “Microheater: material, design, fabrication, temperature control, and applications—a role in COVID-19,” *Biomed. Microdevices*, vol. 24, no. 1, p. 3, Dec. 2021, doi: 10.1007/s10544-021-00595-8.

[4] C.-L. Dai, “A capacitive humidity sensor integrated with micro heater and ring oscillator circuit fabricated by CMOS–MEMS technique,” *Sens. Actuators B Chem.*, vol. 122, no. 2, pp. 375–380, Mar. 2007, doi: 10.1016/j.snb.2006.05.042.

[5] T.-S. Yang and J.-C. Chiou, “A High-Efficiency Driver Circuit for a Gas-Sensor Microheater Based on a Switch-Mode DC-to-DC Converter,” *Sensors*, vol. 20, no. 18, p. E5367, Sep. 2020, doi: 10.3390/s20185367.

[6] J. Han, Z. Tan, K. Sato, and M. Shikida, “Thermal characterization of micro heater arrays on a polyimide film substrate for fingerprint sensing applications,” *J. Micromechanics Microengineering*, vol. 15, no. 2, pp. 282–289, Nov. 2004, doi: 10.1088/0960-1317/15/2/006.

[7] D. Beckel, D. Briand, A. Bieberle-Hütter, J. Courbat, N. F. de Rooij, and L. J. Gauckler, “Micro-hotplates—A platform for micro-solid oxide fuel cells,” *J. Power Sources*, vol. 166, no. 1, pp. 143–148, Mar. 2007, doi: 10.1016/j.jpowsour.2006.12.072.

[8] J. M. Phillips, “Up Close: Nanoscale Science Research Centers,” *MRS Bull.*, vol. 31, no. 1, pp. 45–49, Jan. 2006, doi: 10.1557/mrs2006.5.

[9] K. A. A. Makinwa and J. H. Huijsing, “A smart wind sensor using time-multiplexed thermal Σ Δ modulators,” in *Proceedings of the 27th European Solid-State Circuits Conference*, Sep. 2001, pp. 452–455.

[10] D. Hohlfeld, M. Epmeier, and H. Zappe, “A thermally tunable, silicon-based optical filter,” *Sens. Actuators Phys.*, vol. 103, no. 1, pp. 93–99, Jan. 2003, doi: 10.1016/S0924-4247(02)00320-5.

[11] R. G. Spruit, J. T. van Omme, M. K. Ghatkesar, and H. H. P. Garza, "A Review on Development and Optimization of Microheaters for High-Temperature In Situ Studies," *J. Microelectromechanical Syst.*, vol. 26, no. 6, pp. 1165–1182, Dec. 2017, doi: 10.1109/JMEMS.2017.2757402.

[12] F. Lucklum, A. Schwaiger, and B. Jakoby, "High temperature micro-hotplates on porous silicon substrates," in *2013 Transducers & Eurosensors XXVII: The 17th International Conference on Solid-State Sensors, Actuators and Microsystems (TRANSDUCERS & EUROSENSORS XXVII)*, Jun. 2013, pp. 1907–1910. doi: 10.1109/Transducers.2013.6627165.

[13] N.-K. Song, J.-I. Yun, and S.-K. Joo, "A study on the electrical properties of Pb(Zr, Ti)O3 thin films crystallized by the electrical resistive heating of Pt thin film," *Mater. Res. Bull.*, vol. 43, no. 2, pp. 292–296, Feb. 2008, doi: 10.1016/j.materresbull.2007.03.012.

[14] Md. N. Hasan, D. Acharjee, D. Kumar, A. Kumar, and S. Maity, "Simulation of Low Power Heater for Gas Sensing Application," *Procedia Comput. Sci.*, vol. 92, pp. 213–221, Jan. 2016, doi: 10.1016/j.procs.2016.07.348.

[15] G.-S. Chung and J.-M. Jeong, "Fabrication of micro heaters on polycrystalline 3C-SiC suspended membranes for gas sensors and their characteristics," *Microelectron. Eng.*, vol. 87, no. 11, pp. 2348–2352, Nov. 2010, doi: 10.1016/j.mee.2010.04.005.

[16] M. Prasad, D. S. Arya, and V. K. Khanna, "Fabrication and reliability study of a double spiral platinum-based MEMS hotplate," *J. MicroNanolithography MEMS MOEMS*, vol. 14, p. 025003, Apr. 2015, doi: 10.1117/1.JMM.14.2.025003.

[17] J. Duvigneau, H. Schönherr, and G. J. Vancso, "Nanoscale Thermal AFM of Polymers: Transient Heat Flow Effects," *ACS Nano*, vol. 4, no. 11, pp. 6932–6940, Nov. 2010, doi: 10.1021/nn101665k.

[18] H. Ma, W. Wang, and X. Liu, "Methane detection with high temperature all-silicon microheater," in *2014 IEEE SENSORS*, Nov. 2014, pp. 186–189. doi: 10.1109/ICSENS.2014.6984964.

[19] A. VanHorn and W. Zhou, "Design and optimization of a high temperature microheater for inkjet deposition," *Int. J. Adv. Manuf. Technol.*, vol. 86, no. 9, pp. 3101–3111, Oct. 2016, doi: 10.1007/s00170-016-8440-8.

[20] T. L. Bergman, T. L. Bergman, F. P. Incropera, D. P. DeWitt, and A. S. Lavine, *Fundamentals of Heat and Mass Transfer*. John Wiley & Sons, 2011.

[21] W. M. Haynes, *CRC Handbook of Chemistry and Physics*. CRC Press, 2016.

[22] E. A. Bel'skaya and E. Yu. Kulyamina, "Electrical resistivity of titanium in the temperature range from 290 to 1800 K," *High Temp.*, vol. 45, no. 6, pp. 785–796, Dec. 2007, doi: 10.1134/S0018151X07060090.

[23] P. Bhattacharyya, "Technological Journey Towards Reliable Microheater Development for MEMS Gas Sensors: A Review," *IEEE Trans. Device Mater. Reliab.*, vol. 14, no. 2, pp. 589–599, Jun. 2014, doi: 10.1109/TDMR.2014.2311801.

[24] J. Spannhake *et al.*, "SnO2:Sb – A new material for high-temperature MEMS heater applications: Performance and limitations," *Sens. Actuators B Chem.*, vol. 124, no. 2, pp. 421–428, Jun. 2007, doi: 10.1016/j.snb.2007.01.004.

[25] M. S. Lekshmi, R. Pamula, A. Kartik, and K. J. Suja, "Performance analysis of micro hotplate based metal oxide nanowire gas sensor," in *2018 7th International Symposium on Next Generation Electronics (ISNE)*, May 2018, pp. 1–4. doi: 10.1109/ISNE.2018.8394690.

[26] M. S. Utomo, Y. Whulanza, and G. Kiswanto, "Maskless visible-light photolithography of copper microheater for dynamic microbioreactor," *AIP Conf. Proc.*, vol. 2193, no. 1, p. 050013, Dec. 2019, doi: 10.1063/1.5139386.

[27] L. Sujatha, V. S. Selvakumar, S. Aravind, R. Padamapriya, and B. Preethi, "Design and Analysis of Micro-Heaters for Temperature Optimization using COMSOL Multiphysics for MEMS Based Gas Sensor," 2012. https://www.comsol.com/paper/design-and-analysis-of-micro-heaters-for-temperature-optimization-using-comsol-m-13697 (accessed Jun. 26, 2022).

[28] X. Yi, J. Lai, H. Liang, and X. Zhai, "Fabrication of a MEMS micro-hotplate," *J. Phys. Conf. Ser.*, vol. 276, p. 012098, 2011, doi: 10.1088/1742-6596/276/1/012098.

[29] I. Simon, N. Bârsan, M. Bauer, and U. Weimar, "Micromachined metal oxide gas sensors: opportunities to improve sensor performance," *Sens. Actuators B Chem.*, vol. 73, no. 1, pp. 1–26, Feb. 2001, doi: 10.1016/S0925-4005(00)00639-0.

[30] M. Gharesi and M. Ansari, "Tin Oxide Microheater for Chemical Sensors," vol. 108, p. 012018, Mar. 2016, doi: 10.1088/1757-899X/108/1/012018.

[31] Y. Yang, S. Li, H. Xu, Y. Xu, and Y. Chen, "Fabrication of flexible microheater with tunable heating capabilities by direct laser writing and selective electrodeposition," *J. Manuf. Process.*, vol. 74, pp. 88–99, Feb. 2022, doi: 10.1016/j.jmapro.2021.11.045.

[32] P. Ginet *et al.*, "Towards Single Cell Heat Shock Response by Accurate Control on Thermal Confinement with an On-Chip Microwire Electrode," *Lab. Chip*, vol. 11, pp. 1513–20, Mar. 2011, doi: 10.1039/c0lc00701c.

[33] K.-N. Lee, D.-S. Lee, S. Jung, Y.-H. Jang, Y.-K. Kim, and W.-K. Seong, "A High-temperature MEMS Heater Using Suspended Silicon Structures," *J. Micromechanics Microengineering*, vol. 19, p. 115011, Oct. 2009, doi: 10.1088/0960-1317/19/11/115011.

[34] W.-J. Hwang, K.-S. Shin, J.-H. Roh, D.-S. Lee, and S.-H. Choa, "Development of micro-heaters with optimized temperature compensation design for gas sensors," *Sensors*, vol. 11, no. 3, pp. 2580–2591, 2011, doi: 10.3390/s110302580.

[35] W.-C. Tian, H. K. L. Chan, C.-J. Lu, S. W. Pang, and E. T. Zellers, "Multiple-stage microfabricated preconcentrator-focuser for micro gas chromatography system," *J. Microelectromechanical Syst.*, vol. 14, no. 3, pp. 498–507, Jun. 2005, doi: 10.1109/JMEMS.2005.844842.

[36] S. K. Tiwari, S. Bhat, and K. K. Mahato, "Design and fabrication of screen printed microheater," *Microsyst. Technol.*, vol. 24, no. 8, pp. 3273–3281, Aug. 2018, doi: 10.1007/s00542-018-3821-6.

[37] Z. X. Cai, X. Y. Zeng, and J. Duan, "Fabrication of platinum microheater on alumina substrate by micro-pen and laser sintering," *Thin Solid Films*, vol. 519, no. 11, pp. 3893–3896, Mar. 2011, doi: 10.1016/j.tsf.2011.01.240.

[38] A. Bashir, T. I. Awan, A. Tehseen, M. B. Tahir, and M. Ijaz, "Chapter 3 - Interfaces and surfaces," in *Chemistry of Nanomaterials*, T. I. Awan, A. Bashir, and A. Tehseen, Eds. Elsevier, 2020, pp. 51–87. doi: 10.1016/B978-0-12-818908-5.00003-2.

[39] Y. Xie *et al.*, "Thermally-Reconfigurable Silicon Photonic Devices and Circuits," *IEEE J. Sel. Top. Quantum Electron.*, vol. 26, no. 5, pp. 1–20, Sep. 2020, doi: 10.1109/JSTQE.2020.3002758.

[40] A. H. Atabaki, A. A. Eftekhar, S. Yegnanarayanan, and A. Adibi, "Sub-100-nanosecond thermal reconfiguration of silicon photonic devices," *Opt. Express*, vol. 21, no. 13, pp. 15706–15718, Jul. 2013, doi: 10.1364/OE.21.015706.

[41] A. Masood *et al.*, "CMOS-compatible Tungsten heaters for silicon photonic waveguides," in *The 9th International Conference on Group IV Photonics (GFP)*, Aug. 2012, pp. 234–236. doi: 10.1109/GROUP4.2012.6324144.

[42] A. H. Atabaki, E. Shah Hosseini, A. A. Eftekhar, S. Yegnanarayanan, and A. Adibi, "Optimization of metallic microheaters for high-speed reconfigurable silicon photonics," *Opt. Express*, vol. 18, no. 17, pp. 18312–18323, Aug. 2010, doi: 10.1364/OE.18.018312.

[43] F. Gan *et al.*, “Maximizing the Thermo-Optic Tuning Range of Silicon Photonic Structures,” in *2007 Photonics in Switching*, Aug. 2007, pp. 67–68. doi: 10.1109/PS.2007.4300747.

[44] M. Geng *et al.*, “Four-channel reconfigurable optical add-drop multiplexer based on photonic wire waveguide,” *Opt. Express*, vol. 17, no. 7, pp. 5502–5516, Mar. 2009, doi: 10.1364/OE.17.005502.

[45] P. Dong *et al.*, “Low power and compact reconfigurable multiplexing devices based on silicon microring resonators,” *Opt. Express*, vol. 18, no. 10, pp. 9852–9858, May 2010, doi: 10.1364/OE.18.009852.

[46] P. Dong *et al.*, “Thermally tunable silicon racetrack resonators with ultralow tuning power,” *Opt. Express*, vol. 18, no. 19, pp. 20298–20304, Sep. 2010, doi: 10.1364/OE.18.020298.

[47] Q. Fang *et al.*, “High Efficiency Ring-Resonator Filter With NiSi Heater,” *IEEE Photonics Technol. Lett.*, vol. 24, no. 5, pp. 350–352, Mar. 2012, doi: 10.1109/LPT.2011.2177816.

[48] H.-T. Kim and M. Yu, “High-speed optical sensor interrogator with a silicon-ring-resonator-based thermally tunable filter,” *Opt. Lett.*, vol. 42, no. 7, pp. 1305–1308, Apr. 2017, doi: 10.1364/OL.42.001305.

[49] N. Sherwood-Droz *et al.*, “Optical 4×4 hitless silicon router for optical Networks-on-Chip (NoC),” *Opt. Express*, vol. 16, no. 20, pp. 15915–15922, Sep. 2008, doi: 10.1364/OE.16.015915.

[50] C. Lavoie, F. M. d’Heurle, C. Detavernier, and C. Cabral, “Towards implementation of a nickel silicide process for CMOS technologies,” *Microelectron. Eng.*, vol. 70, no. 2, pp. 144–157, Nov. 2003, doi: 10.1016/S0167-9317(03)00380-0.